Reviews of Electromagnetics, Vol. IV, 2025
EuCAP 2025 Special Issue
DOI: 10.53792/RoE/2025/25007

Reviews of Electromagnetics
EuCAP 2025 Special Issue

Effective-Height Analysis of UWB Antenna Arrays for TDoA and PDoA Estimation

Tobias Lafer[1,2]*, Michael Gadringer[3], Ulrich Muehlmann[1], Franz Teschl[2], Klaus Witrisal[2]

Abstract
State-of-the-art low-power ultra-wideband (UWB) chipsets commonly rely on phase-difference of arrival (PDoA) and time-difference of arrival (TDoA) measurements for performing angle-of-arrival (AoA) estimations. But in real-world scenarios, the TDoA and PDoA measurements suffer from AoA-dependent phase and delay biases introduced by the receiver antennas. If not proerly compenated, the accuracy of the fina AoA estimates reduces. To assess such antenna influences, we extend effective-height-based analysis methods from standalone antennas to antenna arrays for simulation and measurement. Each antenna element is modelled as an LTI system, with its effective height as AoA-dependent transfer function. The obtained effective heights of the single antenna elements consider coupling effects between the antenna elements as well as objects in their vicinity. The proposed simulation and measurement procedures were applied to two different antenna pairs, one composed of directional antennas and one composed of omnidirectional antennas. We compare impulse responses as well as PDoA and TDoA estimates obtained from simulations and measurements to discuss influences of the measurement system as well as modelling uncertainties in the simulation. We found that effecitve heights and PDoAs correlate rather well between simulation and measurement for the investigated antennas. However, substantial differences were observed between simulated and measured TDoAs, which require further investigation.

Key terms
Ultra-Wideband; Angle-of-Arrival; Phase-difference-of-arrival; Effective Height; Antenna impulse response

[1] *NXP Semiconductors Austria, Gratkorn, Austria*
[2] *Institute of Communication Networks and Satellite Communications , Graz University of Technology, Graz, Austria*
[3] *Institute of Microwave and Photonic Engineering , Graz University of Technology, Graz, Austria*
*__Corresponding author__: tobiasflorian.lafer@nxp.com

Received: 22/05/2025, Accepted: 01/09/2025, Published: 28/11/2025

1. Introduction & State-of-the-Art

Modelling and mitigating antenna influences on transmitted and received signals is of special interest for ultra-wideband (UWB) radio systems, which are used for high-accuracy localization. The impacts of bandwidth, array geometry and multipath propagation on the achievable localization accuracy were already subject to extensive investigations [1, 2, 3]. But these investigations neglect the impact of the radiation and reception characteristics of the utilized antenna arrays, although it was shown that non-ideal antenna characteristics can lead to degradations of the localization accuracy [4, 5, 6, 7]. Localization in UWB radio systems can be achieved by exploiting various parameters of the received signals [8], and antennas may impact each of them differently. In low-power UWB chpisets, the estimation of the angle-of-arrival (AoA) of an incident electromagnetic wave is commonly based on phase-difference of arrival (PDoA) and time-difference of arrival (TDoA) measurements [9, 10, 11, 12]. Analyses of antenna influence on these signal parameters were performed by system-level measurements [11, 12] in the past, but were not isolating antenna effects from other performance impairments caused by e.g. the wireless channel. Alternative approaches analyze antenna influences using resource intensive receive-mode simulation procedures [13], requiring the re-execution of full-wave EM simulations if e.g. different polarizations of the incident waves shall be investigated. To circumvent these and other drawbacks of state-of-the-art methods, we propose wideband antenna analysis methods build up on an antenna parameter called *effective height* [6, 14]. The effective

height[1] is a receive-mode antenna parameter, modelling the conversion between field-level and circuit-level quantities in a broadband manner by treating antennas as LTI systems [17]. Provided that reciprocity holds for an investigated antenna, the effective height also fully describes the antenna in transmit mode [14, 18].

Determining the effective height of an antenna by measurement is discussed in [6] and [16]. S-parameter measurements are performed between the antenna under test (AUT) mounted on a suitable positioner, and a reference antenna with sufficient bandwidth and known polarization. The AUTs effective height versus incident wave direction is then determined from the captured transmission S-parameters. The S-parameter measurements were thereby compensated for the propagation channel in the anechoic chamber and the effective height of the reference antenna itself. The reference antenna's effective height is determined by a preceding calibration measurement.

An efficient way for determining effective the height of an AUT from simulation is presented in [19] and [20]. The AUT operates in transmit mode, and its effective height is determined from probing the radiated electric field strength due to a given port voltage. Towards the end of [19], the authors provide a short analysis of different two-antenna arrangements. Last but not least, [13] discusses a simulation approach for determining the PDoA versus AoA relations of a two-antenna arrangement on a UWB sensor node in receive mode. The direction of an incident wave is varied along the xz-cut of the problem domain. For each incident wave direction, a time domain simulation was performed, using a 500MHz UWB pulse as envelope of the incident plane wave. The receivers of the used UWB chipset were modelled as perfect 50Ω resistors, and the PDoA for each incident wave direction was determined by the phase shift between the resulting voltage signals at these resistors.

The current work intends to assess antenna influences on PDoA and TDoA measurements delivered UWB radio systems, using effective-height-based models for the respective antenna arrays. For this purpose, we propose three major contributions to the state-of-the-art: First, the theoretical framework for modelling UWB antenna arrays by means of their effective heights is developed. We do so by extending the derivations from [6], which cover standalone antennas, to antenna arrays. A rather similar derivation was provided in the recent paper [21], but considering narrowband arrays only, and thus omitting any form of time-domain analysis.
Based on the derived array model, we introduce a wideband signal model for analyzing direction-of-arrival and polarization dependent array influences on the received signals, as a basis for subsequent PDoA and TDoA measurements. To the best knowledge of the authors, this signal model together with the PDoA/TDoA analysis methodology have not been presented in the literature so far. The developed signal model and analysis methodology are applicable to effective-height models determined from either simulations or measurements. The second major contribution of the current paper is therefore the extension of the simulation schemes from [19] and [20] to antenna arrays. Utilizing the reciprocity property of the investigated antennas, the desired antenna effective heights can be determined from transmit mode simulations and applied in subsequent receive mode analyses. This approach circumvents two major drawbacks of direct receive mode analysis procedures carried out in, e.g., [13]. The first drawback is the increasing simulation effort with a growing number of incident wave directions, an issue already brought up by the authors of [19] as an argument for performing a transmit mode analysis rather than a receive mode analysis. Secondly, the simulation results are tied to the selected polarization of the incident wave, leading to a further increase in the computational effort if the impact of an incident wave's polarization shall be investigated. However, the effective-height-based approach introduced in our work allows arbitrary incident wave polarizations to be analyzed without requiring additional EM simulations. Determining the effective height of a single antenna by measurement is covered [6] for the 2D case, and extended to 3D measurements in [16].
As third and last major contribution of our paper, we propose generalizations of these measurement techniques to antenna arrays. In contrast to [6] and [16], we use a 6-axis robot arm for rotating the AUT in the three-dimensional space while keeping the reference antenna static. This allows to keep the relative position between the AUT and the reference antenna constant upon rotation, which is of special importance when comparing simulated and measured effective heights of the AUT. The impact of not rotating around an AUTs apparent phase center in measurement[2], is shortly addressed [6] and can be circumvented with our proposed measurement setup as well.

The rest of the paper is organized as follows: Section 2 provides the mathematical framework for effective-height-based antenna modelling and analysis. A revisit of the necessary basics is provided in Section 2.1, due to unfortunately inconsistent definitions and notations of the effective height and related formulas found in literature [6, 14, 18]. The proposed extensions to the array case are then discussed in Subsections 2.2, 2.3 and 2.4. The calculation steps to obtain the desired PDoA and TDoA measurements from antenna port voltages sensed by UWB receivers are covered in Section 3. Sections 4 and 5 discuss the proposed methods for determining antenna effective heights in the array case in simulation and measurement. Finally, simulation and measurement results are provided in Section 6, together with a detailed discussion. Appendices A and B provide background information on the coordinate system conventions used during simulation and measurements, as well as adapted PDoA and TDoA relations for planar arrays under this coordinate system conventions.

2. Effective-height-based characterization of multi-antenna arrangements

2.1. Standalone antenna

The *effective height* $\boldsymbol{H} \in \mathbb{C}^3$ of an antenna is a receive-mode model parameter, describing the conversion of the electric field strength of a incident plane electromagnetic to the respective outward propagating voltage wave at the antenna port. A corre-

[1] Alternative names for the *effective height* found in literature are *(vector) effective length* [15] or *antenna transfer function* [16].

[2] Provided that one exists and does not significantly move with frequency.

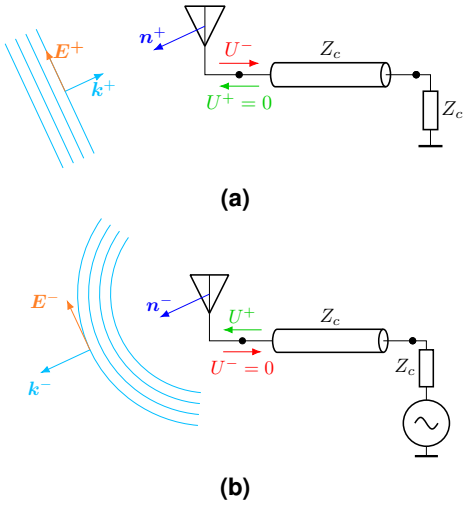

Figure 1: Receive and transmit mode relations for a standalone antenna. In receive mode (a), the antenna is terminated with a matched load ($U^+ = 0$), whereas in transmit mode (b), the antenna is fed from a matched source ($U^- = 0$).

sponding sketch is found in Figure 1a. The electric field strength of the plane wave is denoted as $\boldsymbol{E}^+ \in \mathbb{C}^3$, and its propagation vector is $\boldsymbol{k}^+ = -\frac{2\pi}{\lambda}\boldsymbol{n}^+$. The outward propagating voltage wave at the antenna port is denoted as $U^- \in \mathbb{C}$.

$$\frac{U^-(\omega,\boldsymbol{n}^+)}{\sqrt{Z_c}} = \boldsymbol{H}^H(\omega,\boldsymbol{n}^+)\cdot\frac{\boldsymbol{E}^+(\omega,\boldsymbol{n}^+)}{\sqrt{Z_0}}\,, \tag{1}$$

Superscript ^{H} denotes Hermitian transposition, ω is the angular frequency in rad s^{-1}, λ is the wavelength, $Z_0 \in \mathbb{R}^+$ is the free space impedance, $Z_c \in \mathbb{R}^+$ denotes the reference impedance associated with S-parameter measurements at the antenna port[3] and $\boldsymbol{n}^+ \in \mathbb{R}^3$ is a unit vector denoting the incident wave direction. The effective height $\boldsymbol{H}$ is always related to a geometrically fixed reference point on the antenna structure, which can be freely selected[4]. The electric field strength $\boldsymbol{E}^+$ in (1) is then the electric field strength of the incident plane wave exactly at this reference point. In the time domain, (1) becomes

$$\frac{u^-(t,\boldsymbol{n}^+)}{\sqrt{Z_c}} = \boldsymbol{h}^T(t,\boldsymbol{n}^+) * \frac{\boldsymbol{e}^+(t,\boldsymbol{n}^+)}{\sqrt{Z_0}}\,, \tag{2}$$

with $u^- \in \mathbb{R}$ and $\boldsymbol{h},\boldsymbol{e}^+ \in \mathbb{R}^3$. The time domain equivalent $\boldsymbol{h}(t,\boldsymbol{n}^+)$ of the effective height $\boldsymbol{H}(\omega,\boldsymbol{n}^+)$ is commonly known as the *antenna impulse response* or *antenna transient response*. The $*$ operator in (2) is a composition of an inner product and a convolution:

$$\boldsymbol{f}^T(t) * \boldsymbol{g}(t) := \int_{-\infty}^{\infty} \boldsymbol{f}(\tau)^T \cdot \boldsymbol{g}(t-\tau)\,d\tau\,. \tag{3}$$

In transmit mode, depicted in Figure 1b, a vector-valued dimensionless transmit factor $\boldsymbol{A} \in \mathbb{C}^3$ relates an incident voltage wave at the antenna port $U^+ \in \mathbb{C}$ from a matched source, to the electric field strength $\boldsymbol{E}^- \in \mathbb{C}^3$ of the resulting radiated electromagnetic wave with propagation vector $\boldsymbol{k}^- = \frac{2\pi}{\lambda}\boldsymbol{n}^-$. The respective frequency domain relation is

$$\frac{\boldsymbol{E}^-(\omega,r,\boldsymbol{n}^-)}{\sqrt{Z_0}} = \frac{1}{r}e^{-j\omega\frac{r}{c_0}}\boldsymbol{A}(\omega,\boldsymbol{n}^-)\frac{U^+(\omega)}{\sqrt{Z_c}}\,, \tag{4}$$

with r and $\boldsymbol{n}^-$ being distance and direction from the selected reference point on the antenna to an arbitrary observation point, and c_0 denoting the speed of light. One derives again an equivalent time domain relation

$$\frac{\boldsymbol{e}^-(t,r,\boldsymbol{n}^-)}{\sqrt{Z_0}} = \frac{1}{r}\delta\left(t-\frac{r}{c_0}\right) * \boldsymbol{a}(t,\boldsymbol{n}^-) * \frac{u^+(t)}{\sqrt{Z_c}}\,. \tag{5}$$

If the antenna is reciprocal, $\boldsymbol{h}$ and $\boldsymbol{a} \in \mathbb{R}^3$ are related by [14, 18, 22]

$$\boldsymbol{a} = \frac{1}{2\pi c_0}\frac{\partial}{\partial t}\boldsymbol{h} \tag{6}$$

in the time domain, and equivalently in the frequency domain by

$$\boldsymbol{A} = \frac{j\omega}{2\pi c_0}\boldsymbol{H}\,. \tag{7}$$

Applying the reciprocity relations (6) and (7) to the time- and frequency domain transmit mode relations (4) and (5) delivers

$$\frac{\boldsymbol{E}^-(\omega,r,\boldsymbol{n}^-)}{\sqrt{Z_0}} = \frac{j\omega}{2\pi c_0 r}e^{-j\omega\frac{r}{c_0}}\boldsymbol{H}(\omega,\boldsymbol{n}^-)\frac{U^+(\omega)}{\sqrt{Z_c}}\,, \tag{8}$$

and

$$\begin{aligned}\frac{\boldsymbol{e}^-(t,r,\boldsymbol{n}^-)}{\sqrt{Z_0}} &= \frac{1}{2\pi c_0 r}\delta\left(t-\frac{r}{c_0}\right) * \frac{\partial \boldsymbol{h}(t,\boldsymbol{n}^-)}{\partial t} * \frac{u^+(t)}{\sqrt{Z_c}} \\ &= \frac{1}{2\pi c_0 r}\delta\left(t-\frac{r}{c_0}\right) * \boldsymbol{h}(t,\boldsymbol{n}^-) * \frac{1}{\sqrt{Z_c}}\frac{\partial u^+(t)}{\partial t}\,,\end{aligned} \tag{9}$$

due to the properties of the convolution operator.

If the radiated electric field strength of an antenna due to a certain excitation voltage is known, (8) allows to determine an antennas effective height via

$$\boldsymbol{H}(\omega,\boldsymbol{n}^-) = \frac{2\pi c_0 r}{j\omega}e^{j\omega\frac{r}{c_0}}\sqrt{\frac{Z_c}{Z_0}}\frac{\boldsymbol{E}^-(\omega,r,\boldsymbol{n}^-)}{U^+(\omega)}\,. \tag{10}$$

2.2. Extension to antenna arrays

Provided that linearity holds, all relations from Section 2.1 apply for the array case depicted in Figure 2 as well. The transmit mode relation of single antenna m in the array case, depicted in Figure 2b, is then similar to the transmit mode relation in the standalone case, if all other antennas are terminated with matched loads:

$$\frac{\boldsymbol{E}_m^-(\omega,r_m,\boldsymbol{n}_m^-)}{\sqrt{Z_0}} = \frac{j\omega}{2\pi c_0 r_m}e^{-j\omega\frac{r_m}{c_0}}\boldsymbol{H}_m(\omega,\boldsymbol{n}_m^-)\frac{U_m^+(\omega)}{\sqrt{Z_c}}\Bigg|_{\substack{U_l^+=0\\ \forall l\in[1\ldots M],l\neq m}}\,. \tag{11}$$

[3] Z_c is also assumed to be the wave impedance of all transmission lines attached to the antenna ports.

[4] Common reference point selections are geometric center of the antenna structure or, if known in advance, the phase center of the antenna.

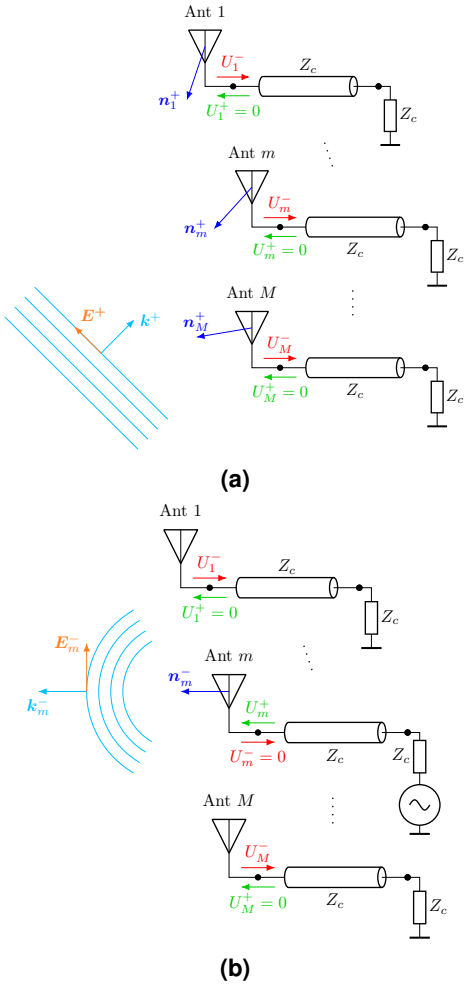

Figure 2: Receive and transmit-mode relations for antenna arrays. In receive mode, (a) all antennas are terminated with matched loads. In transmit mode, (b) the currently active antenna m is fed from a matched source, while all other antennas are terminated with matched loads.

The receive mode relation of antenna m, depicted in Figure 2a, is

$$\frac{U_m^-(\omega,\boldsymbol{n}_m^+)}{\sqrt{Z_c}} = \boldsymbol{H}_m^H(\omega,\boldsymbol{n}_m^+)\cdot\frac{\boldsymbol{E}_m^+(\omega,\boldsymbol{n}_m^+)}{\sqrt{Z_0}}\bigg|_{\substack{U_m^+=0\\ \forall m\in[1\ldots M]}}, \tag{12}$$

provided that all antennas are terminated with matched loads. Mutual coupling between antennas, as well as coupling to objects in proximity, are implicitly modelled by the effective heights in (11) and (12).

Relation (11) allows to determine the effective height of antenna m by probing the radiated electric field strength due to a given excitation voltage, similar to (10):

$$\boldsymbol{H}_m(\omega,\boldsymbol{n}_m^-) = \tag{13}$$
$$= \frac{2\pi c_0 r_m}{j\omega}e^{-j\omega\frac{r_m}{c_0}}\sqrt{\frac{Z_c}{Z_0}}\frac{\boldsymbol{E}_m^-(\omega,r_m,\boldsymbol{n}_m^-)}{U_m^+(\omega)}\bigg|_{\substack{U_l^+=0\\ \forall l\in[1\ldots M],l\neq m}}$$

Relation (13) will be used in Section 4.1, when determining an antenna's effective height from simulation.

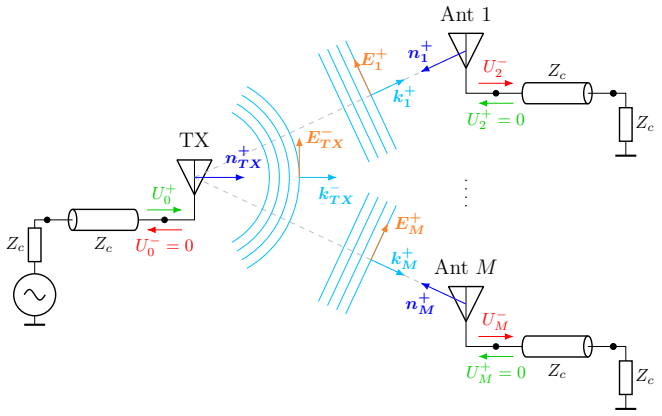

Figure 3: SIMO wireless link. The transmit antenna is fed from a matched source, while all receive antennas are terminated with matched loads.

2.3. The SIMO wireless link

When interpreting the single-input-multi-output (SIMO) radio link depicted in Figure 3 as a multiport circuit, the respective transmission S-parameters between the antenna ports can be expressed in terms of the effective heights of the involved antennas. Assuming that the same reference impedance Z_c is applied at all antenna ports, the relation between the excitation voltage U_0^+ at the TX antenna and the resulting port voltage U_m^- at receive antenna m is obtained by combining (8) and (12):

$$U_m^-(\omega,r_m,\boldsymbol{n}_m^+) = \tag{14}$$
$$= \frac{j\omega}{2\pi c_0 r_m}e^{-j\omega\frac{r_m}{c_0}}\boldsymbol{H}_m^H(\omega,\boldsymbol{n}_m^+)\cdot\boldsymbol{H}_0(\omega,-\boldsymbol{n}_m^+)U_0^+(\omega)\,.$$

Interpreting the SIMO wireless link as a multiport circuit, relation (14) describes the respective transmission S-parameters S_{m0} between the TX and RX antenna ports:

$$S_{m0}(\omega,r_m,\boldsymbol{n}_m^+) = \frac{U_m^-}{U_0^+} = \tag{15}$$
$$= \frac{j\omega}{2\pi c_0 r_m}e^{-j\omega\frac{r_m}{c_0}}\boldsymbol{H}_m^H(\omega,\boldsymbol{n}_m^+)\cdot\boldsymbol{H}_0(\omega,-\boldsymbol{n}_m^+).$$

Equation (15) is important for determining an antenna's effective height by measurement, further described in Section 5.

2.4. Array signal model

Having proper wideband antenna models at hand, the next step is to develop parametric data models for the signals sensed by UWB receivers at the antenna ports, which are further used for direction finding via PDoA and TDoA measurements. For this purpose, the setup depicted in Figure 4 is considered, in addition to the following assumptions:

A1 (Matched Receivers)**.** The UWB receivers are perfectly matched to the antenna ports, i.e, each of the M receivers is capable of acquiring $\boldsymbol{U}_m^-$ without impairments.

A2 (Far-Field conditions)**.** Far-field conditions are assumed, i.e. the distance between transmit antenna and receive antenna array is large enough, such that all receive antennas observe a plane wave incident from direction $\boldsymbol{n}^+$ [23].

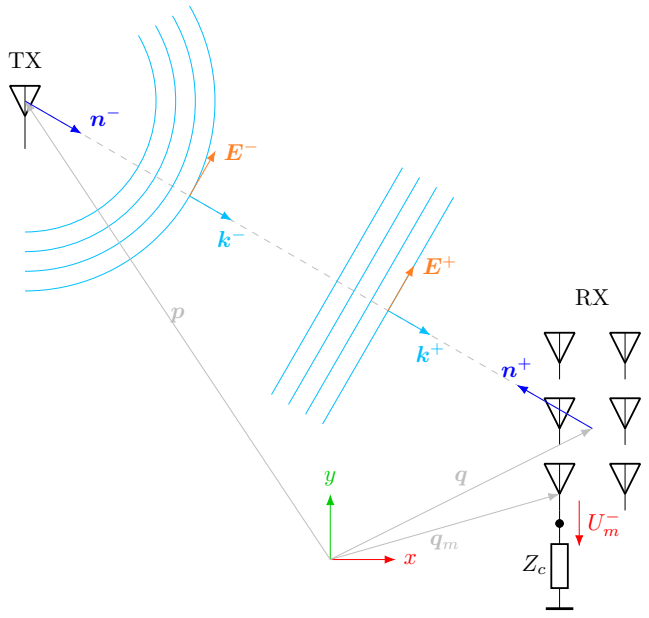

Figure 4: SIMO antenna link from Figure 3 under the far-field assumption A2.

A3 (Ideal transmit antenna)**.** The transmit antenna is an ideal isotropic radiator with infinite bandwidth.

A4 (Bandpass excitation)**.** The excitation signal on the TX side is assumed to be a bandlimited lowpass signal $s(t) \in \mathbb{C}$, up-converted to the desired RF band with angular center frequency ω_0.

The transmit antenna at position $\boldsymbol{p} \in \mathbb{R}^3$ emits an electromagnetic wave propagating towards an array of M receive antennas at positions $\boldsymbol{q}_m \in \mathbb{R}^3$, $m = 0 \ldots M-1$. Due to assumption A2, the incident direction $\boldsymbol{n}^+$ and the propagation direction $\boldsymbol{n}^-$ can be expressed as

$$\boldsymbol{n}^- = -\boldsymbol{n}^+ = \frac{\boldsymbol{q}-\boldsymbol{p}}{r_{qp}} , \tag{16}$$

with $\boldsymbol{q}$ being the *array reference point*

$$\boldsymbol{q} = \frac{1}{M}\sum_{m=1}^{m} \boldsymbol{q}_m, \tag{17}$$

and $r_{qp} = \|\boldsymbol{q}-\boldsymbol{p}\|$. We further introduce $\Delta\boldsymbol{q}_m = \boldsymbol{q}_m - \boldsymbol{q}$ as the position of antenna element m relative to the array reference point.

Due to assumption A3, the TX antenna's effective height $\boldsymbol{H}_{\mathrm{TX}}$ is proportional to the polarization $\boldsymbol{P}$ of the emitted electromagnetic wave:

$$\begin{aligned}\boldsymbol{H}_{\mathrm{TX}}\left(\omega,\boldsymbol{n}^-\right) &\propto \boldsymbol{P}(\omega,\boldsymbol{n}^-) = \\ &= P_\varphi e^{j\mathrm{sign}(\omega)\phi_\varphi}\boldsymbol{i}_\varphi(\boldsymbol{n}^-) + P_\theta e^{j\mathrm{sign}(\omega)\phi_\theta}\boldsymbol{i}_\theta(\boldsymbol{n}^-) ,\end{aligned} \tag{18}$$

where the propagation direction $\boldsymbol{n}^-$ points in radial direction, and $\boldsymbol{i}_\varphi$ and $\boldsymbol{i}_\theta$ are the respective unit vectors in azimuth and elevation direction. Consequently, $\boldsymbol{P}^H(\omega,\boldsymbol{n}^-)\cdot\boldsymbol{n}^- \equiv 0$. The parameters P_φ, P_θ, ϕ_φ and ϕ_θ are real numbers determining the polarization state [15, Sec. 2.12]. As the radiated electric field strength is a real-valued quantity in the time-domain, the sign(ω) terms are required in (18) to maintain Hermitian symmetry of $\boldsymbol{H}_{\mathrm{TX}}$ in frequency domain. See Appendix A for further details. Combining (18) and (11), the radiated electric field strength at distance r from the TX antenna is

$$\frac{\boldsymbol{E}^-(\omega,r,\boldsymbol{n}^-)}{\sqrt{Z_0}} = \frac{j\omega}{2\pi c_0 r} e^{-j\omega\frac{r}{c_0}} \boldsymbol{P}(\omega,\boldsymbol{n}^-)\frac{U_0^+(\omega)}{\sqrt{Z_c}} . \tag{19}$$

The electric field strength (19) leads to receive antenna port voltages

$$\begin{aligned}U_m^-(\omega,\boldsymbol{n}^+) &= \\ &= \frac{j\omega}{2\pi c_0\|\boldsymbol{q}_m-\boldsymbol{p}\|} e^{-j\omega\frac{\|\boldsymbol{q}_m-\boldsymbol{p}\|}{c_0}} \boldsymbol{H}_m^H(\omega,\boldsymbol{n}^+)\cdot\boldsymbol{P}(\omega,-\boldsymbol{n}^+)U_0^+(\omega) ,\end{aligned} \tag{20}$$

according to (14), whereby $\boldsymbol{n}^- = -\boldsymbol{n}^+$ has been considered.

Next, the far-field assumption A2 is used to further simplify (20). The path losses towards all M receive antennas can be assumed to be similar, leading to

$$\frac{1}{\|\boldsymbol{q_m}-\boldsymbol{p}\|} \to \frac{1}{r_{qp}} . \tag{21}$$

In addition, as a plane wave incident on the antenna array is assumed, the complex exponential can be rephrased in terms of the incident wave direction $\boldsymbol{n}^+$ as following [23]:

$$e^{-j\omega\frac{\|\boldsymbol{q}_m-\boldsymbol{p}\|}{c_0}} \to e^{-j\omega\frac{\boldsymbol{n}^-\cdot(\boldsymbol{q}_m-\boldsymbol{p})}{c_0}} = e^{j\omega\frac{\boldsymbol{n}^+\cdot(\boldsymbol{q}_m-\boldsymbol{p})}{c_0}} \tag{22}$$

Further considering $\boldsymbol{q}_m = \boldsymbol{q} + \Delta\boldsymbol{q}_m$ delivers

$$e^{j\omega\frac{\boldsymbol{n}^+\cdot(\Delta\boldsymbol{q}_m+\boldsymbol{q}-\boldsymbol{p})}{c_0}} = e^{j\omega\frac{\boldsymbol{n}^+\cdot\Delta\boldsymbol{q}_m}{c_0}} e^{j\omega\frac{\boldsymbol{n}^+\cdot(\boldsymbol{q}-\boldsymbol{p})}{c_0}} = e^{j\omega\frac{\boldsymbol{n}^+\cdot\Delta\boldsymbol{q}_m}{c_0}} e^{-j\omega\tau} \tag{23}$$

with

$$\tau := -\frac{\boldsymbol{n}^+\cdot(\boldsymbol{q}-\boldsymbol{p})}{c_0} \tag{24}$$

being propagation delay between the transmit antenna and the reference point of the receive antenna array. Using simplifications (21) - (23) in (20) yields

$$\begin{aligned}U_m^-(\omega,\boldsymbol{n}^+) &= \\ &= \frac{j\omega}{2\pi c_0 r_{qp}} e^{j\omega\frac{\boldsymbol{n}^+\cdot\Delta\boldsymbol{q}_m}{c_0}} e^{-j\omega\tau} \boldsymbol{H}_m^H(\omega,\boldsymbol{n}^+)\cdot\boldsymbol{P}(\omega,-\boldsymbol{n}^+)U_0^+(\omega) .\end{aligned} \tag{25}$$

Last but not least, assumption A4 is considered. The signal $s(t)$ is assumed to be a baseband signal, with spectrum $S(\omega) := \mathscr{F}\{s(t)\}$ and $S(\omega) = 0 + j0 \;\forall\; |\omega| > B$, whereby parameter B denotes the signal's bandwidth in rad s^{-1} and $\mathscr{F}$ is the Fourier transform. The TX antenna port voltage is obtained from up-converting $s(t)$ to the desired RF channel with angular center frequency ω_0 and taking the real part, which in time-domain leads to

$$u_0^+(t) = Re\left\{s(t)e^{j\omega_0 t}\right\} . \tag{26}$$

For convenience in the upcoming derivations, u_0^+ is expressed by its complex pre-envelope $\hat{u}_0^+$, which is obtained from u_0^+ using the Hilbert transform $\mathscr{H}$:

$$\hat{u}_0^+(t) := u_0^+(t) + j\mathscr{H}\left\{u_0^+(t)\right\} = s(t)e^{j\omega_0 t} \tag{27}$$

The spectrum of $\hat{u}_0^+$ is

$$\hat{U}_0^+(\omega) := \mathscr{F}\left\{\hat{u}_0^+(t)\right\} = S(\omega-\omega_0)\,, \tag{28}$$

and is a bandpass spectrum with non-zero frequency components only within $\omega_0 - B \le \omega \le \omega_0 + B$. The resulting bandpass spectra of the receive antenna port voltages are

$$\hat{U}_m^-(\omega,\boldsymbol{n}^+) = \tag{29}$$
$$= \frac{j\omega}{2\pi c_0 r_{qp}} e^{j\omega\left(\frac{\boldsymbol{n}^+\cdot\Delta\boldsymbol{q}_m}{c_0}-\tau\right)} \boldsymbol{H}_m^H(\omega,\boldsymbol{n}^+)\cdot\boldsymbol{P}(\omega,-\boldsymbol{n}^+)S(\omega-\omega_0).$$

Down-conversion of $\hat{U}_m^-$ delivers the equivalent lowpass spectra

$$\tilde{U}_m^-(\omega,\boldsymbol{n}^+) := \hat{U}_m^-(\omega+\omega_0,\boldsymbol{n}^+) = \tag{30}$$
$$= \frac{j(\omega+\omega_0)}{2\pi c_0 r_{qp}} e^{j(\omega+\omega_0)\left(\frac{\boldsymbol{n}^+\cdot\Delta\boldsymbol{q}_m}{c_0}-\tau\right)} \tilde{\boldsymbol{H}}_m^H(\omega,\boldsymbol{n}^+)\cdot\tilde{\boldsymbol{P}}(\omega,-\boldsymbol{n}^+)\,S(\omega),$$

with non-zero frequency components only within $|\omega| \le B$ and

$$\tilde{\boldsymbol{H}}_m(\omega,\boldsymbol{n}^+) := \boldsymbol{H}_m(\omega+\omega_0,\boldsymbol{n}^+)$$
$$\tilde{\boldsymbol{P}}(\omega,-\boldsymbol{n}^+) := \boldsymbol{P}(\omega+\omega_0,-\boldsymbol{n}^+)$$

denoting the lowpass spectra of the receive antenna effective height and transmit antenna polarization respectively. However, polarization $\tilde{\boldsymbol{P}}$ is independent of ω in baseband, as

$$\tilde{\boldsymbol{P}}(\omega,-\boldsymbol{n}^+) = P_\varphi e^{j\mathrm{sign}(\omega+\omega_0)\phi_\varphi}\boldsymbol{i}_\varphi(-\boldsymbol{n}^+) + P_\theta e^{j\mathrm{sign}(\omega+\omega_0)\phi_\theta}\boldsymbol{i}_\theta(-\boldsymbol{n}^+)\,, \tag{31}$$

and $\mathrm{sign}(\omega+\omega_0) = 1\ \forall\ |\omega| \le B \le \omega_0$. Formally dropping the frequency dependence of $\tilde{\boldsymbol{P}}$,

$$\tilde{\boldsymbol{P}}(\omega,-\boldsymbol{n}^+) \to \tilde{\boldsymbol{P}}(-\boldsymbol{n}^+) = P_\varphi e^{j\phi_\varphi}\boldsymbol{i}_\varphi(-\boldsymbol{n}^+) + P_\theta e^{j\phi_\theta}\boldsymbol{i}_\theta(-\boldsymbol{n}^+)\,, \tag{32}$$

delivers the final expression for the baseband spectra of the receive antenna port voltages:

$$\tilde{U}_m^-(\omega,\boldsymbol{n}^+) = \tag{33}$$
$$= \frac{j(\omega+\omega_0)}{2\pi c_0 r_{qp}} e^{j(\omega+\omega_0)\left(\frac{\boldsymbol{n}^+\cdot\Delta\boldsymbol{q}_m}{c_0}-\tau\right)} \tilde{\boldsymbol{H}}_m^H(\omega,\boldsymbol{n}_m^+)\cdot\tilde{\boldsymbol{P}}(-\boldsymbol{n}^+)\,S(\omega)$$

One can further collect all M port voltages (33) in a single vector

$$\tilde{\boldsymbol{U}}^-(\omega,\boldsymbol{n}^+) := \begin{bmatrix}\tilde{U}_1^-(\omega,\boldsymbol{n}^+)\\ \tilde{U}_2^-(\omega,\boldsymbol{n}^+)\\ \vdots \\ \tilde{U}_M^-(\omega,\boldsymbol{n}^+)\end{bmatrix} = \tag{34}$$
$$= \tilde{\boldsymbol{H}}_{\mathrm{RX}}(\omega,\boldsymbol{n}^+)\cdot\frac{j(\omega+\omega_0)\tilde{\boldsymbol{P}}(-\boldsymbol{n}^+)}{2\pi c_0 r_{qp}} e^{-j(\omega+\omega_0)\tau} S(\omega)$$

where all receive-antenna related terms are collected in a single matrix $\tilde{\boldsymbol{H}}_{\mathrm{RX}} \in \mathbb{C}^{M\times 3}$, called *antenna reception matrix* in the following:

$$\tilde{\boldsymbol{H}}_{\mathrm{RX}}(\omega,\boldsymbol{n}^+) := \begin{bmatrix}\tilde{\boldsymbol{H}}_1^H(\omega,\boldsymbol{n}^+)e^{j(\omega+\omega_0)\frac{\boldsymbol{n}^+\cdot\Delta\boldsymbol{q}_1}{c_0}}\\ \tilde{\boldsymbol{H}}_2^H(\omega,\boldsymbol{n}^+)e^{j(\omega+\omega_0)\frac{\boldsymbol{n}^+\cdot\Delta\boldsymbol{q}_2}{c_0}}\\ \vdots \\ \tilde{\boldsymbol{H}}_M^H(\omega,\boldsymbol{n}^+)e^{j(\omega+\omega_0)\frac{\boldsymbol{n}^+\cdot\Delta\boldsymbol{q}_M}{c_0}}\end{bmatrix} \tag{35}$$

Considering that the terms next to $\tilde{\boldsymbol{H}}_{\mathrm{RX}}$ in (34) are baseband representations of the incident plane wave's electric field strength at the array reference point,

$$\frac{j(\omega+\omega_0)\tilde{\boldsymbol{P}}(-\boldsymbol{n}^+)}{2\pi c_0 r_{qp}} e^{-j(\omega+\omega_0)\tau} S(\omega) \triangleq \boldsymbol{E}^+(\omega+\omega_0,\boldsymbol{n}^+)$$
$$:= \tilde{\boldsymbol{E}}^+(\omega,\boldsymbol{n}^+)\,, \tag{36}$$

relation (34) can be interpreted as a generalization of the receive mode relation (1) for antenna arrays under a plane-wave assumption:

$$\tilde{\boldsymbol{U}}^-(\omega,\boldsymbol{n}^+) = \tilde{\boldsymbol{H}}_{\mathrm{RX}}(\omega,\boldsymbol{n}^+)\cdot\tilde{\boldsymbol{E}}^+(\omega,\boldsymbol{n}^+)\,. \tag{37}$$

3. Baseband processing

The final step required for analyzing the impact of antennas on PDoA and TDoA measurements, is to consider the actual processing steps performed within a UWB receiver to obtain the desired PDoA and TDoA measurements from the antenna port voltages (33). For notational convenience, we introduce

$$\tau_m := -\frac{\boldsymbol{n}^+\cdot\Delta\boldsymbol{q}_m}{c_0} + \tau\,, \tag{38}$$

with τ_m expressing the propagation delay from the transmitter to receiving antenna m and τ from (24). The minus signs in (38) are a consequence of the incident direction $\boldsymbol{n}^+$ pointing in the opposite direction than the propagation vector $\boldsymbol{k}^+$ of the respective incident wave (see Figure 4). With (38), one obtains for the time-domain equivalents of the antenna port voltages (33)

$$\tilde{u}_m^-(t,\boldsymbol{n}^+) = \frac{j\omega_0}{2\pi c_0 r_{qp}} e^{-j\omega_0\tau_m}\left\{\tilde{\boldsymbol{P}}^H\cdot\dot{\tilde{\boldsymbol{h}}}_m * s\right\}\left(t-\tau_m,\boldsymbol{n}^+\right)\,, \tag{39}$$

using definitions

$$\tilde{\boldsymbol{h}}_m(t,\boldsymbol{n}^+) := \mathscr{F}^{-1}\left\{\tilde{\boldsymbol{H}}_m(\omega,\boldsymbol{n}^+)\right\}\,, \tag{40}$$
$$\dot{\tilde{\boldsymbol{h}}}_m(t,\boldsymbol{n}^+) := \frac{d}{dt}\tilde{\boldsymbol{h}}_m(t,\boldsymbol{n}^+)\,. \tag{41}$$

The dot-product between polarization $\tilde{\boldsymbol{P}}$ and antenna impulse response $\tilde{\boldsymbol{h}}_m$ reveals that the receive antenna acts as the weighted sum of linear filters. The respective filter impulse responses are determined by $\tilde{\boldsymbol{h}}_m$, whereas polarization $\tilde{\boldsymbol{P}}$ determines the weights. As a consequence of the antenna impulse response $\tilde{\boldsymbol{h}}_m$

being a direction dependent quantity, the total filtering operation applied the antenna is generally direction and polarization dependent. Antenna effects being direction and polarization depends is known to the literature [24, 25]. However, the current works differs from [24, 25] in the sense that the direction and polarization dependent antenna effects are now to considered to vary within the bandwidth of the received signal as well, i.e. the common assumption of the signal bandwidth being much smaller than the antenna bandwidth is not applied.

From (39), one observes that the port voltage of antenna m in time-domain is essentially determined by the baseband excitation signal on the TX side, $s(t)$, delayed by the propagation delay τ_m and filtered by the time derivative of the antenna impulse response $\dot{\tilde{\boldsymbol{h}}}_m$. These filtering operations add deterministic, but generally direction and polarization dependent delays to the signals at the antenna ports. Consequently, the delay estimations performed in UWB radio systems for localization purposes are subject to a direction and polarization dependent bias term, denoted by $\hat{\tau}_m$ in the following.

Delay estimations in low-power UWB chipsets are commonly achieved by relatively simple algorithms due to the lack of available computation power. One example is a matched filter followed by a peak-search algorithm [26, 27]. The output of such a matched filter is, when applied to the port voltages (39),

$$y_m(t,\boldsymbol{n}^+) = \tilde{u}_m^-(t,\boldsymbol{n}^+) * s(-t) = \\ = \frac{j\omega_0}{2\pi c_0 r_{qp}} e^{-j\omega_0\tau_m} \left\{ \tilde{\boldsymbol{P}}^H \cdot \dot{\tilde{\boldsymbol{h}}}_m * R_{ss} \right\}(t-\tau_m) \,, \tag{42}$$

with R_{ss} being the autocorrelation function of $s(t)$. Targeting the analysis of the antenna-induced delay bias term $\hat{\tau}_m$ as a deterministic effect, no form of noise or multipath propagation is considered in the antenna port voltages (39). The total signal delay or *time-of-arrival (ToA)* T_m at antenna m is now estimated by searching for the magnitude peak of the matched filter output:

$$T_m(\boldsymbol{n}^+,\tilde{\boldsymbol{P}}) := \underset{t}{\operatorname{argmax}} \left| y_m(t,\boldsymbol{n}^+) \right| = \\ \triangleq \tau_m + \hat{\tau}_m(\boldsymbol{n}^+,\tilde{\boldsymbol{P}}) = -\frac{\boldsymbol{n}^+ \cdot \Delta\boldsymbol{q}_m}{c_0} + \tau + \hat{\tau}_m(\boldsymbol{n}^+,\tilde{\boldsymbol{P}}) \tag{43}$$

The phase of the matched filter output at the magnitude peak location, frequently called *phase-of-arrival (PoA)* Φ_m, can also be expressed as the sum of a true PoA ϕ_m determined only by the array geometry, and an antenna-induced bias term $\hat{\phi}_m$:

$$\Phi_m(\boldsymbol{n}^+,\tilde{\boldsymbol{P}}) := \arg\left\{ y(T_m,\boldsymbol{n}^+) \right\} \triangleq \phi_m + \hat{\phi}_m \tag{44}$$

considering that $\frac{\omega_0}{c_0} = \frac{2\pi}{\lambda}$. The true PoA ϕ_m is thereby the phase of (42), neglecting the filtering operation through the antenna:

$$\phi_m := \pi - \omega_0\tau_m = \pi + \frac{2\pi\, \boldsymbol{n}^+ \cdot \Delta\boldsymbol{q}_m}{\lambda} - \omega_0\tau \,. \tag{45}$$

With (45), one finally obtains for (44)

$$\Phi_m(\boldsymbol{n}^+,\tilde{\boldsymbol{P}}) = \pi + \frac{2\pi\, \boldsymbol{n}^+ \cdot \Delta\boldsymbol{q}_m}{\lambda} - \omega_0\tau + \hat{\phi}_m(\boldsymbol{n}^+,\tilde{\boldsymbol{P}}) \,. \tag{46}$$

The true ToA τ_m in (43) and the true PoA ϕ_m in (46) offer a linear relationship

$$\phi_m = \pi - \omega_0\tau_m \,. \tag{47}$$

A similar relationship does not necessarily exist for the delay and phase bias terms $\hat{\tau}_m$ and $\hat{\phi}_m$, especially if the effective height of the respective antenna shows a strong nonlinear phase within the bandwidth of the received signal. And even if such a relationship would exists for one incident direction and polarization, this may not be the case for all incident directions and polarizations. As a consequence, the final ToA estimates T_m from (43) and PoA estimates from (46) do not offer a generally valid relationship similar to (47).

The true ToAs τ_m at each of the M antennas are only determined by the array geometry and the incident wave direction $\boldsymbol{n}^+$ according to (38). Consequently, if one is capable of precisely determining the ToAs from multiple antennas, the incident wave direction $\boldsymbol{n}^+$ can be estimated from the pairwise ToA differences, the *Time-Difference-of-Arrival (TDoA)* ΔT_{nm} [9]. The TDoA between two antennas n and m is obtained as

$$\Delta T_{nm} := T_n - T_m = \\ = -\frac{\boldsymbol{n}^+ \cdot (\Delta\boldsymbol{q}_n - \Delta\boldsymbol{q}_m)}{c_0} + \hat{\tau}_n(\boldsymbol{n}^+,\tilde{\boldsymbol{P}}) - \hat{\tau}_m(\boldsymbol{n}^+,\tilde{\boldsymbol{P}}). \tag{48}$$

For real world antennas, the delay bias terms $\hat{\tau}_n$ and $\hat{\tau}_m$ in (48) do not necessarily cancel out for all incident wave directions $\boldsymbol{n}^+$ and polarizations $\tilde{\boldsymbol{P}}$. Hence, the resulting TDoA measurements are also subject to direction and polarization dependent bias.

The incident wave direction $\boldsymbol{n}^+$ may alternatively be estimated from pairwise differences between the PoA of two antennas, the *Phase-difference-of-arrival (PDoA)*:

$$\Delta\Phi_{nm} = \Phi_n - \Phi_m = \\ = \frac{2\pi\, \boldsymbol{n}^+ \cdot (\Delta\boldsymbol{q}_n - \Delta\boldsymbol{q}_m)}{c_0} + \hat{\Phi}_n(\boldsymbol{n}^+,\tilde{\boldsymbol{P}}) - \hat{\Phi}_m(\boldsymbol{n}^+,\tilde{\boldsymbol{P}}) \tag{49}$$

Similar as for the TDoAs, the PDoA measurements may be subject to a direction- and polarization dependent bias, if the phase bias terms $\hat{\Phi}_n$ and $\hat{\Phi}_m$ do not cancel out for all $\boldsymbol{n}^+$ and $\tilde{\boldsymbol{P}}$.

4. Simulation Framework

4.1. Determining antenna effective heights from Full-Wave EM simulations

The fundamental equation for determining an antenna's effective height from full-wave EM simulation results is (13). Following this equation, one requires the electric field strength radiated by an antenna due to a specific excitation voltage sampled on a spherical surface and exported from the simulation software.

An example simulation model is shown in Figure 5, showing two co-polarized *crossed exponentially tapered slot (XETS)* antennas [19] with a separation of 40mm, created in Ansys HFSS [28] version 2024R1. The two sub-figures depict the distribution of the spatial E-field samples points around the antennas, in line with the sampling point distribution of the

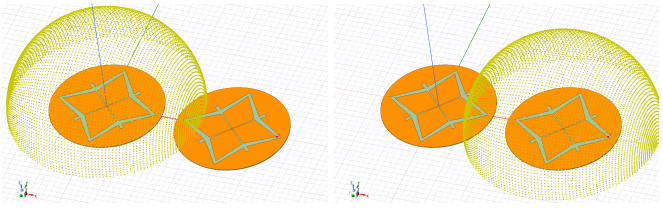

(a) (b)

Figure 5: Model of a XETS antenna pair in Ansys HFSS. A *near field sphere* is spanned up around the center of each antenna. The distribution of the E-field sample points on each sphere was selected in alignment with the sample point in measurement. For visualization purposes, the radii of the sample points were reduced from 1m to 30mm.

measurement procedure later introduced in Section 5. The center points of the sphere surfaces were set to the geometric centers of the respective antennas, although the selection of arbitrary center points is possible[5]. Last but not least, the radii of the spherical surfaces must be large enough to ensure far-field conditions. The sphere radii in Figure 5 were reduced to 30mm for visualization purposes; the final simulations were executed with a radius of 1m.

If the simulation domain contains multiple antennas, e.g. as shown in Figure 5, the antennas are sequentially excited with an incident voltage wave of $U_m^+ = (1+j0)\text{V}$, while all other antennas are terminated with matched loads. The radiated electric field strength of the currently active is then sampled at the desired spatial sampling points, and applied in (13) to obtain the desired effective height. It shall be emphasized that the effective height determined in this way implicitly contains effects due to mutual coupling between the antennas, or other unwanted effects due to e.g. coupling to objects in proximity. The simulation frequency range for all antennas covered in this document was $[2\text{GHz}, 12\text{GHz}]$ with a step width of 5MHz. A raised-cosine filter is applied to the effective heights determined from the E-field sample points, for the purpose of circumventing long ringing in respective antenna impulse responses due to the finite simulation frequency range. The roll-off factor of the raised-cosine filter was selected to set the transient bands to the $[2\text{GHz}, 4\text{GHz}]$ and $[10\text{GHz}, 12\text{GHz}]$ intervals.

4.2. Simulating PDoA and TDoA measurements

Having determined the effective heights of the antenna array under test, the desired PDoA and TDoA measurements are obtained by following the calculation steps discussed in Sections 2.4 and 3. A root-raised cosine pulse with a roll-off factor of 0.5 and a low-pass bandwidth of 250MHz is considered as baseband excitation signal $s(t)$ in (27) and (42). This pulse-shape is equivalent to the baseband reference pulse defined for the *HRP UWB* physical layer specification in [29]. As a next step, the antenna port voltages are calculated according to (39). If not stated otherwise, the polarization $\tilde{\boldsymbol{P}}$ is selected to match the polarization of the antenna under test.

[5] It is however important that the center points in simulation and measurement are equal.

The resulting port voltage is fed to the matched filter (42), followed by the estimation of the time-of-arrival (43) and phase-of-arrival (46).

5. Measurement Setup

The measurement principle follows to a large extent the principle introduced in [6]. The reference antenna is kept static, and the AUT is rotated using a 6 axis robot as shown in Figure 6. A two-port measurement is performed[6] between the reference antenna and each AUT in a multi-antenna setup, with the unused antennas being terminated with matched loads. As shown in Figure 8, only the effective height component co-polarized of the reference antenna's effective height $\boldsymbol{H}_{ref}$ can be determined in a single measurement run. Mathematically, the inner product in (15) vanishes, and one obtains the transmission S-parameter [6, 30]

$$S_{21}(\omega, \boldsymbol{n}^+) = \frac{j\omega}{2\pi c_0 r} e^{-j\omega\frac{r}{c_0}} H_{ref}^*(\omega) H_{AUT,copol}(\omega, \boldsymbol{n}^+) \,, \tag{50}$$

with $H_{AUT,copol}$ denoting the co-polarized effective height component of the AUT. Relation (50) is finally rephrased to determine $H_{AUT,copol}$ from

$$H_{AUT,copol}(\omega, \boldsymbol{n}^+) = \frac{2\pi c_0 r}{j\omega} e^{j\omega\frac{r}{c_0}} \frac{S_{21}(\omega, \boldsymbol{n}^+)}{H_{ref}^*(\omega)} \,. \tag{51}$$

The calculation of $H_{AUT,copol}$ from (51) requires the effective height of the reference antenna H_{ref} to be known. Thus, a calibration measurement is performed with a reference antenna mounted on both ends of the measurement setup. From this measurement, one obtains H_{ref} as

$$H_{ref}(\omega) = \sqrt{\frac{2\pi c_0 r}{j\omega} e^{j\omega\frac{r}{c_0}} S_{21}(\omega)} \,. \tag{52}$$

A raised-cosine filter is applied to the effective heights determined by measurement, similar to the effective heights determined from simulation. To counter unwanted effects caused by e.g. reflections at the 6-axis robot, a window function is further applied to the measured effective heights in the time domain. A Tukey window [31] has been selected for this purpose, as its shape parameter allows a precise selection of the time interval that should not be affected by the window function. A window length of 5ns with a shape factor 0.1 was determined empirically.

The robot used for positioning the AUT is a bench-top 6-axis robot of type *Nova 5* from vendor *Dobot* [32]. A close-up picture of the robot is found in Figure 7. The robot acts as an *elevation-over-azimuth* positioner [33], leading to the azimuth φ and elevation θ rotation angles as shown in Figure 8. Using the robot's built-in inverse kinematics functionality, each of the AUTs could be rotated in space while keeping the reference points selected in simulation (see Figure 5) stationary in space.

[6] One can obviously perform a multi-port measurement as well instead of multiple two-port measurements, assuming that the reference impedances at all ports are identical.

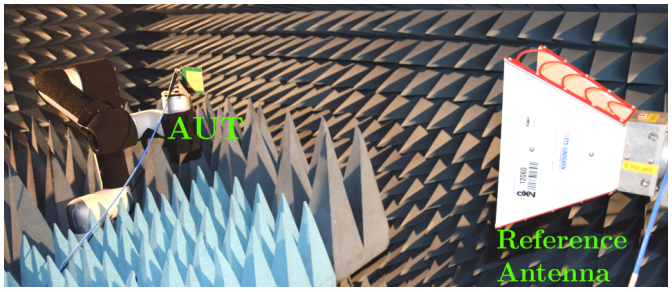

Figure 6: Measurement setup at NXP Semiconductors in Gratkorn, Austria. A 6-axis robot with mounted Vivaldi antenna is depicted, together with a double-ridged horn antenna visible in the front. The entire setup is placed in an anechoic chamber.

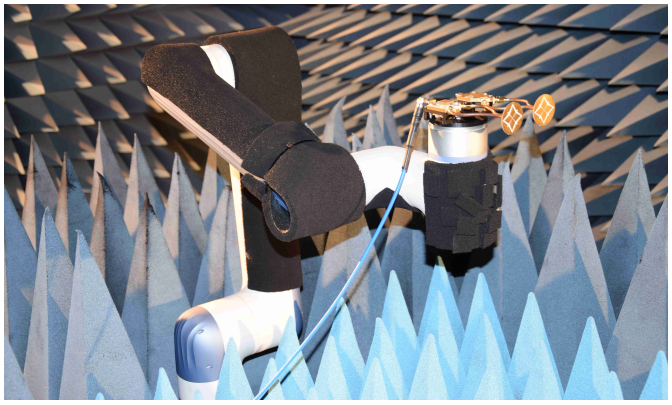

Figure 7: Close-up picture of the 6-axis robot. The XETS antenna pair from Figure 18b is mounted on the robot for example purposes. The robot itself has been covered with flat absorber material wherever possible without affecting the rotary joints.

The robot was additionally covered with flat absorber material wherever possible without affecting the rotary joints, to at least slightly reduce reflections at the robot structure exposed to the radiated field of the reference antenna. A systematic reflection hot-spot analysis as introduced in e.g. [34] can be considered as future research topic, to further reduce the influence of the robot on the measurement results. The remaining details of the measurement setup are:

- **Reference Antenna**: Double-Ridged Guide Horn Antenna, Model 3115 from ETS-Lindgren [35].
- **Vector Network Analyzer & Instrument Settings**: Keysight FieldFox Microwave Analyzer, Type N9916B [36]. The setup was calibrated using an electronic calibration module of type N7553A [37] from Keysight as well. The calibration kit is specified up to -15dBm maximum input power, so all measurements were carried out at this power level. The measured frequency range was $[2\text{GHz}, 12\text{GHz}]$ with a step width of 5MHz. The VNA's IF bandwidth was set to 1kHz.

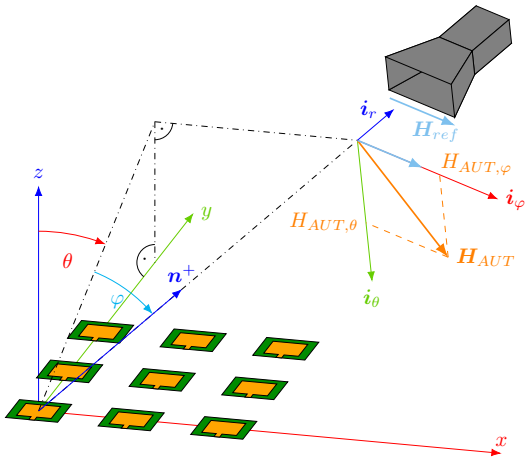

Figure 8: Desired versus measured effective height. Two measurement runs may be required if the alignment between the effective heights of the AUT and the reference antenna are unknown, or the AUTs effective height shows a significant variation over the incident wave direction $\boldsymbol{n}^+$.

6. Simulation & Measurement results

The simulation and measurement procedures introduced in the previous sections were applied to

- the Vivaldi antenna from [38], and
- the XETS-antenna introduced in [19].

A standalone antenna element as well as a pair of antennas with specific spacing has been analyzed for each of the two antenna types above. The PDoA and TDoA measurements delivered by each antenna pair were estimated at *HRP UWB PHY* Channel 5 [29], with a center frequency of ≈ 6.5GHz. All presented results utilize the coordinate system conventions and angle definitions from Appendix A. The PDoA and TDoA relations (49) and (48) for planar and linear arrays under these coordinate system conventions are provided in Appendix B.

6.1. Vivaldi Antenna & Vivaldi Antenna Pair

Figures 9 and 10 depict the simulation models and corresponding measurement assemblies for a standalone Vivaldi antenna and a Vivaldi antenna pair with 30mm spacing respectively. The simulation models consider the 3D-printed antenna fixture from measurement, as well as a short metal cylinder modelling the end-effector of the 6-axis robot. The antenna fixture is made from PLA plastic, and the robot end-effector is considered to be made from aluminum. The vivaldi antennas are dominantly polarized in elevation direction ($\boldsymbol{i}_\theta$ in Figure 8). The reference antenna in measurement as well as the polarization of the incident plane wave in simulation were aligned accordingly.

6.1.1. Results

Figure 11a depicts the elevation component H_θ of the simulated effective height $\boldsymbol{H}$, for a wave incident from direction $\varphi = \theta = 0°$. The unwrapped phase of H_θ together with the thereof derived group delay are depicted in Figures 11b and 11c respectively. Figure 11d depicts antenna impulse response h_θ, derived from H_θ, together with its envelope $|\tilde{h}_\theta|$. A comparison between impulse responses obtained from simulation

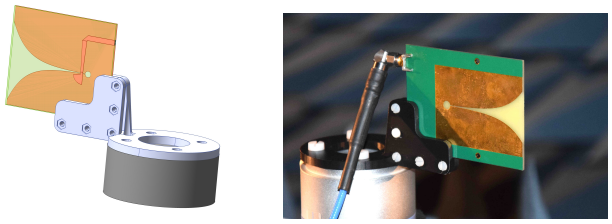

(a) (b)

Figure 9: Standalone Vivaldi antenna in (a) simulation and (b) measurement.

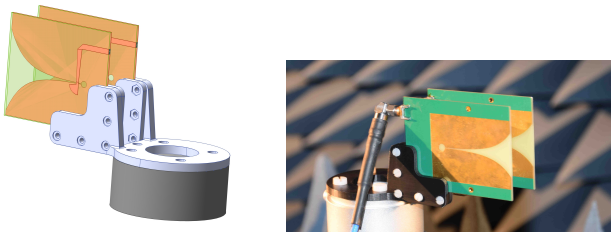

(a) (b)

Figure 10: Vivaldi antenna pair with 30mm spacing in (a) simulation and (b) measurement.

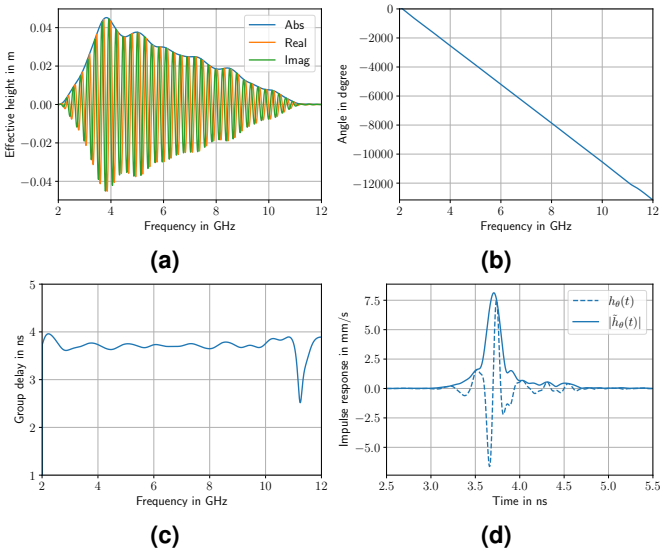

(a) (b) (c) (d)

Figure 11: (a) Simulated elevation component H_θ of the standalone Vivaldi antenna's effective height towards direction $\varphi = \theta = 0°$. Subplot (b) shows the unwrapped phase and subplot (c) the respective group delay. The impulse response h_θ together with its envelope $|\tilde{h}_\theta|$ is shown in (d).

and measurement for is provided in Figure 12 two different incident wave directions. Figure 13a plots the simulated impulse response envelopes $|\tilde{h}_\theta|$ over azimuth φ in the elevation $\theta = 0°$ plane. The respective impulse response envelopes from measurement are depicted in Figure 13b. On the other hand, Figure 14 provides the impulse response envelopes $|\tilde{h}_\theta|$ over elevation θ in the azimuth $\varphi = 0°$ plane. Figures 15(a)-(h) compare simulated and measured PDoAs over azimuth φ for the vivaldi antenna pair from Figure 10. Four different elevation angles $\theta \in \{-30°, 0°, 30°, 60°\}$ were analyzed. The left column shows the PDoA curves wrapped to a $\pm 180°$ interval, whereas the right column depicts the unwrapped PDoAs. In a similar manner, TDoA results from simulation and measurement for the four elevation angles $\theta \in \{-30°, 0°, 30°, 60°\}$ are plotted in Figure 16.

6.1.2. Discussion

The impulse responses depicted in Figures 12 - 14 correlated well between simulation and measurement. However, the measured impulse response in Figure 12b shows a small sidelobe around 4.4ns, which is not present in the simulated impulse response. Possible explanations for this this sidelobe include reflections at the robot structure not modelled in simulation, or reflections at the reference antenna structure scattered back to the AUT. But the latter explanation can be excluded, as in that case a similar sidelobe is expected to be present in Figure 12a, which is not the case. The by far most interesting property of the Vivaldi antenna impulse responses is the formation precursors towards larger azimuth angles. This effect is consistent with measurements performed for a similar Vivaldi antenna in [6]. Such precursors in the antenna impulse responses may lead to a signal dispersion similar to two-path propagation channels [39] for waves incident for the respective directions, even if the actual propagation channel is an AWGN channel.

The PDoA curves depicted in Figures 15a-h show a relatively good correlation between simulations and measurements. However, an increasing mismatch can be observed towards the outer azimuth regions, and for increasing elevation angles. Such mismatches could be expected to a certain extent, due to the directivity of Vivaldi antennas. That is, reflections at the robot structure may become more and more prominent for larger azimuth angles compared to the line-of-sight component. Unfortunately, the correlation between simulated and measured TDoAs depicted in Figures 16a-d is pretty poor, which is quite surprising considering the good correlation of impulse responses and PDoAs discussed before. Another interesting fact about the depicted TDoA curves is, that even the simulated curves do not really follow the expected sinusoidal shape. A drastic example of this effect is Figures 16c, where even the curvatures of the respective simulated and measured TDoA curves change over azimuth. But TDoA curves looking worse than the respective PDoA curves from the same antenna pair have already observed in the past, e.g. in [9]. There, the authors compare the measured PDoA and TDoA curves delivered by an UWB evaluation kit. The PDoA curve follows it's expected sinusoidal shape relatively well, whereas the TDoA curve deviates much stronger from the expected sinusoid.

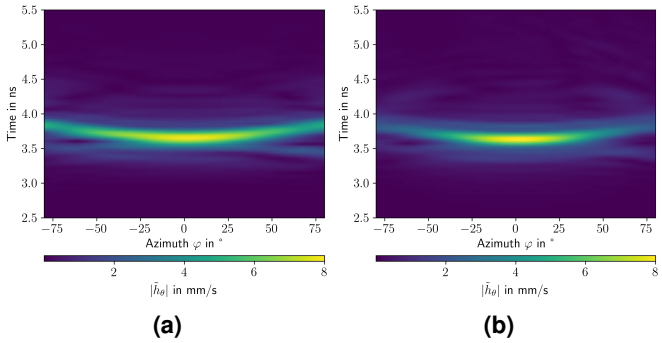

Figure 13: (a) Simulated and (b) measured impulse response envelopes $|\tilde{h}_\theta|$ of the standalone Vivaldi antenna from Figure 9 over azimuth φ at elevation $\theta = 0°$.

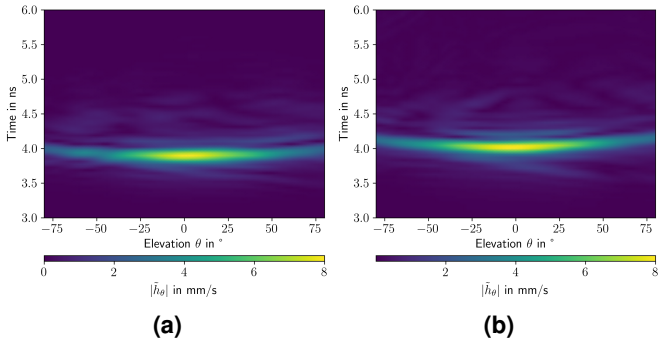

Figure 14: (a) Simulated and (b) measured impulse response envelopes $|\tilde{h}_\theta|$ of the standalone Vivaldi antenna from Figure 9 over elevation θ at azimuth $\varphi = 0°$.

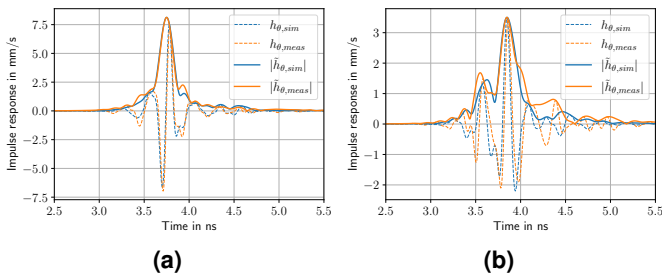

Figure 12: Simulated vs. measured impulse responses h_θ and envelopes $|\tilde{h}_\theta|$ of the standalone Vivaldi antenna from Figure 9 towards (a) $\varphi = \theta = 0°$ and (b) $\varphi = 60°, \theta = 0°$.

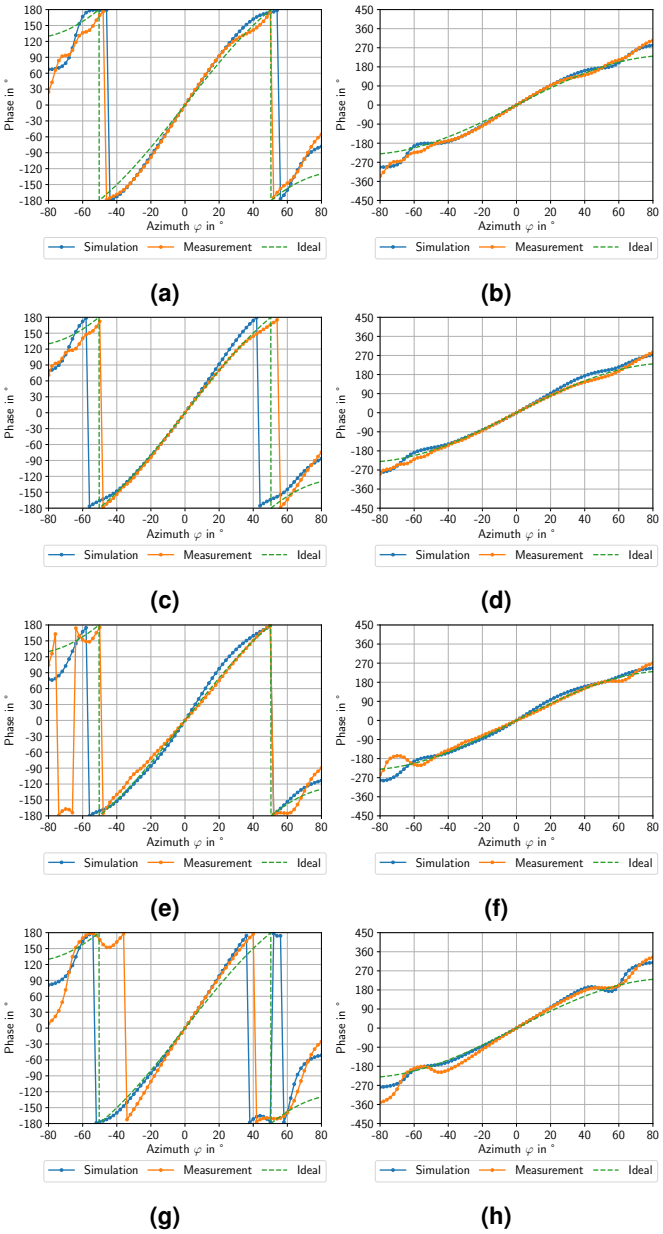

Figure 15: Comparison of simulated and measured PDoA curves over azimuth φ for the Vivaldi antenna pair, measured at UWB channel 5. The rows correspond to different elevation angles of the incident wave. From top to bottom: $\theta = [0°, 30°, 60°, -30°]$. Wrapped curves are depicted in the left column; unwrapped curves in the right column.

6.2. XETS Antenna & XETS Antenna Pair

The second antenna being investigated is the XETS antenna introduced in [19]. Simulation and measurement results are compared for a single antenna element shown in Figure 17, as well as a two-antenna arrangement with a spacing of 57mm shown in Figure 18.

The XETS antenna is essentially a dipole structure that requires symmetric feeding. The authors of [19] considered a single-ended feeding during their measurements, and observed asymmetries in the measured magnitude and phase patterns. The asymmetries were explained by the suboptimal single-ended feeding of the antenna during the measurements. Similar observations were made during initial measurements for the current work, leading to the decision to switch to a symmetrical antenna feeding for the upcoming analysis. A balun model *SCTX1-83-2W+* from *Mini-Circuits* [40] has been selected to provide the symmetrical antenna feeding, due to its large bandwidth and the availability of an evaluation board. But although the selected balun is a 1 : 1 transformer designed for transforming 50Ω single-ended impedance on the input side to a 50Ω differential impedance at the output, the respective evaluation board has 50Ω SMA ports for each of the differential output lines. The differential mode propagating towards the antenna therefore ob-

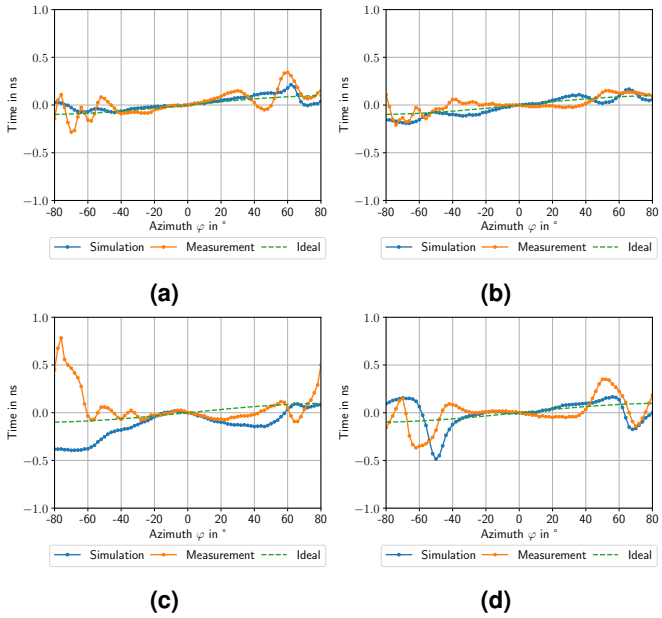

Figure 16: Comparison of simulated and measured TDoA curves over azimuth φ for the Vivaldi antenna pair, measured at UWB channel 5. Subplot (a) shows the PDoA curves for $\theta = 0°$, (b) for $\theta = 30°$, (c) for $\theta = 60°$, and (d) for $\theta = -30°$.

serves a wave impedance larger than the desired 50Ω, leading to reflections at the antenna port with again 50Ω differential impedance. In simulation, the balun was modelled a block of brass, with similar dimensions as the balun evaluation board in measurement. The brass block has two cylindrical cutouts for two coaxial lines depicted in Figure 19a. Each coaxial line is designed to have a single-ended wave impedance of 25Ω. PTFE was considered as insulator, with a relative permittivity of 2.1, and copper was considered as material for the inner and outer conductors. Due to being isolated adequately by design, the wave impedance of the differential mode is 50Ω. Last but not least, the transition from the differential coaxial lines is modelled as shown in Figure 19b, to be as close as possible to coax-to-antenna transition in measurement. The measurements were performed again from 2GHz to 12GHz, although the balun's upper frequency limit is 8GHz. But the PDoA and TDoA measurements were performed at UWB channel 5, with a center frequency of ≈ 6.5GHz, which is still within the balun's specification limits. The XETS antennas are dominantly polarized in azimuth direction ($\boldsymbol{i}_\varphi$ in Figure 8). The reference antenna in measurement as well as the polarization of the incident plane wave in simulation were aligned accordingly.

6.2.1. Results

Figures 20 to 25 follow essentially the Figures discussed already for the Vivaldi antenna(s). Figures 20a-d depict the azimuth component H_φ of the simulated effective height $\boldsymbol{H}$, together with its unwrapped phase, group delay and impulse response in direction $\varphi = \theta = 0°$. A comparison between impulse responses h_φ and envelopes $|\tilde{h}_\varphi|$ obtained from simulation and measurement for two different incident wave directions is provided in Figures 21a-b. The impulse response envelopes $|\tilde{h}_\varphi|$ in

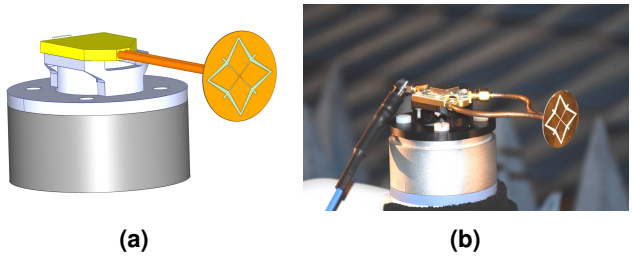

Figure 17: A single XETS in simulation and measurement. The antenna was symmetrically fed using a balun of type *SCTX1-83-2W+* from *MiniCircuits*.

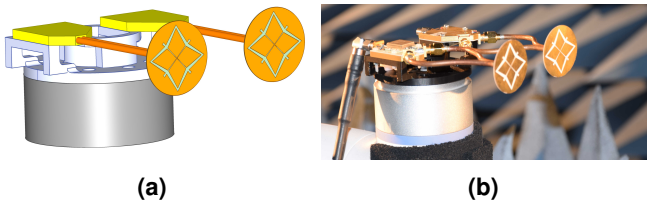

Figure 18: An arrangement of two-antenna XETS arrangement with 57mm spacing in simulation and measurement.

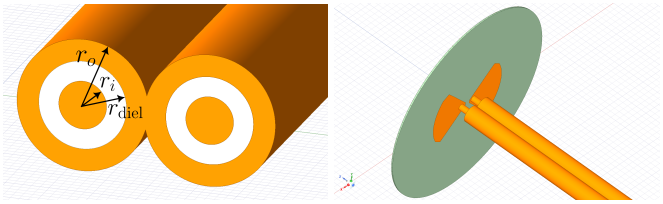

Figure 19: (a) Pair of coaxial transmission lines for providing the required differential feeding for XETS in simulation. (b) Transition from the coaxial transmission line pair to the antenna port. The parameters of each coaxial line are $r_i = 0.545$mm, $r_{\text{diel}} = 1$mm and $r_o = 1.5$mm

the $\theta = 0°$ and $\varphi = 0°$ cuts obtained from simulation and measurement are found in Figures 22a-b and 23a-b. PDoA results are found in Figures 24a-h, and respective TDoA measurements are depicted in Figure 24.

6.2.2. Discussion

The impulse response h_φ in Figure 20d shows a longer ringing compared to the impulse response of the Vivaldi antenna from Figure 11d. The generally longer ringing compared to the Vivaldi antenna can also be observed in Figures 21a-b. The ringing is likely to be caused by reflections at the antenna fixture, due to the XETS antenna having a strong radiation towards it rear side. On the other hand, one observes in the measured antenna impulse response, depicted in Figure 21b, a sidelobe around 5ns which is not present in the respective simulated impulse response. A similar effect was observed for the impulse responses of the Vivaldi antenna depicted in Figure 12, which hardens the assumption that this may be an artifact from reflections of the robot structure not modelled in simulation. The PDoA and TDoA results of the XETS antenna pair are depicted in Figures

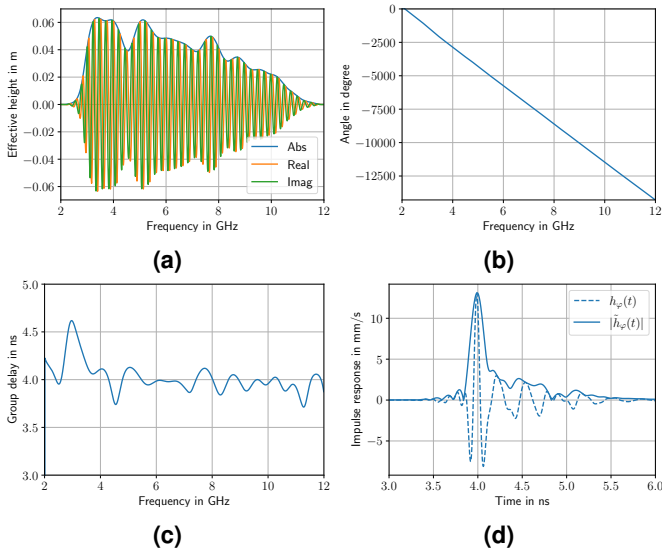

Figure 20: Simulated (a) azimuth component H_φ of the standalone XETS antenna's effective height towards direction $\varphi = \theta = 0°$. Subplot (b) shows the unwrapped phase and subplot (c) the respective group delay. The impulse response h_φ together with its envelope $|\tilde{h}_\varphi|$ is shown in (d).

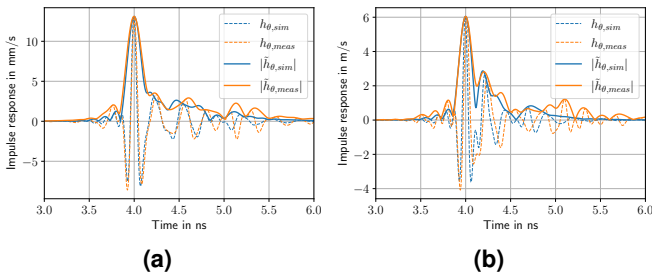

Figure 21: Comparison of simulated and measured impulse responses of a standalone XETS antenna, for an electromagnetic wave incident from direction $\varphi \in [0°, 60°]$, $\theta = 0°$.

24 to 25. A quite good correlation between simulation and measurement is visible for the PDoA curves, whereas poor correlation is observed for the TDoA results. Even in simulation, the TDoA curves are also here far from their ideal sinusoidal shape.

7. Conclusion

The objective of this paper was to extend effective-height based antenna analysis methods to antenna arrays, for assessing antenna influences on PDoA and TDoA measurements. The effective heights determined by the proposed transmit-mode simulation correlate rather well with respective heights determined from measurements. A similar observation was made regarding the correlation between PDoA measurements from simulation and measurement, although even better correlation is expected when closing remaining modelling gaps in then simulation. Unfortunately, only poor correlation between simulation and measurement has been achieved for TDoA, which was a

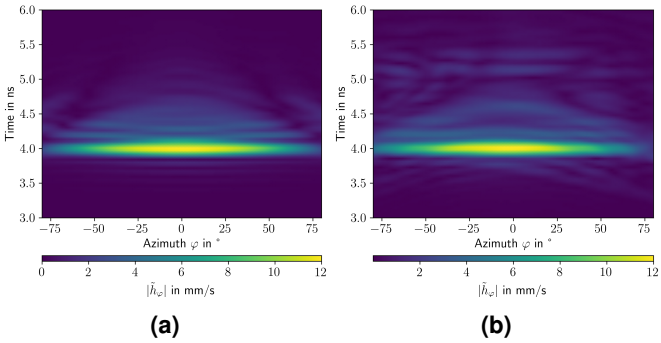

Figure 22: (a) Simulated and (b) measured impulse response envelopes $|\tilde{h}_\varphi|$ of the standalone XETS antenna from Figure 17 over azimuth φ at elevation $\theta = 0°$.

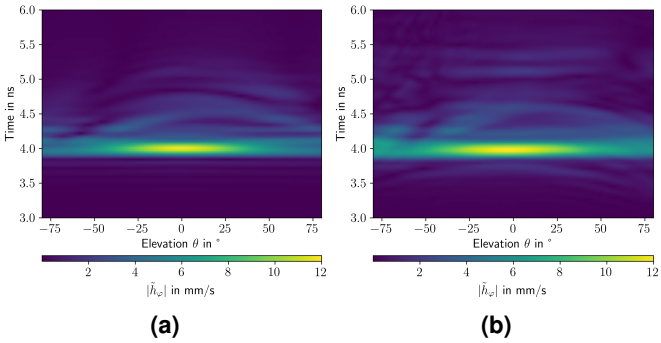

Figure 23: (a) Simulated and (b) measured impulse response envelopes $|\tilde{h}_\varphi|$ of the standalone XETS antenna from Figure 17 over elevation θ at azimuth $\varphi = 0°$.

surprising result considering the good correlation achieved for impulse responses and PDoA. Another very surprising outcome of the TDoA investigations is that the TDoA curves determined from simulation and measurement are in general far off from their expected sinusoidal shape. An explanation for this effect is considered to be subject for further research.

Acknowledgment

The work presented in this document was conducted in the frame of the SINFONIA project. The SINFONIA has received funding from the Recovery and Resilience Facility (RRF) as the centrepiece of NextGenerationEU via the Austrian Research Promotion Agency (FFG) and Austria Wirtschaftsservice Gesellschaft mbH (aws) in the frame of the IPCEI ME/CT – Important Project of Common European Interest on Microelectronic and Communication Technologies under FFG project No 917423 and AWS project No P2431566.

A. Measurement Coordinate System & Modelling of Incident Waves

In the array signal model (33), the baseband representation of the plane waves electric field strength $\tilde{\boldsymbol{E}}^+$ incident on the

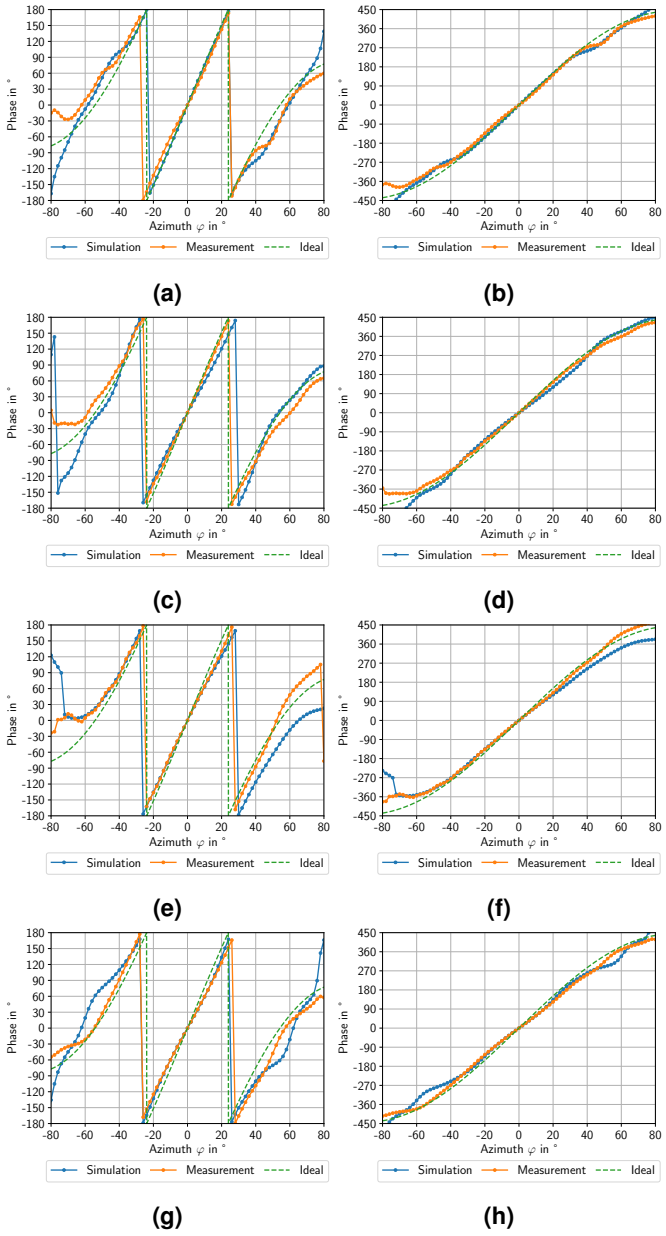

Figure 24: Comparison of simulated and measured PDoA curves over azimuth φ for the XETS antenna pair, measured at UWB channel 5. The rows correspond to different elevation angles of the incident wave. From top to bottom: $\theta = [0°, 30°, 60°, -30°]$. Wrapped curves are depicted in the left column; unwrapped curves in the right column.

antenna array, is according to (36)

$$\tilde{\boldsymbol{E}}^{+}(\omega, \boldsymbol{n}^{+}) = \frac{j(\omega+\omega_0)\,\tilde{\boldsymbol{P}}(-\boldsymbol{n}^{+})}{2\pi c_0 r_{qp}} e^{-j(\omega+\omega_0)\tau} S(\omega)\ , \quad (53)$$

with polarization

$$\tilde{\boldsymbol{P}}(-\boldsymbol{n}^{+}) = P_\varphi e^{j\phi_\varphi} \boldsymbol{i}_\varphi(-\boldsymbol{n}^{+}) + P_\theta e^{j\phi_\theta} \boldsymbol{i}_\theta(-\boldsymbol{n}^{+})\ , \quad (54)$$

according to (32). An illustration is found in Figure 26. The four parameters P_φ, P_θ, ϕ_φ and ϕ_θ in (54) determine the polarization state of the plane wave [15, Ch. 2]:

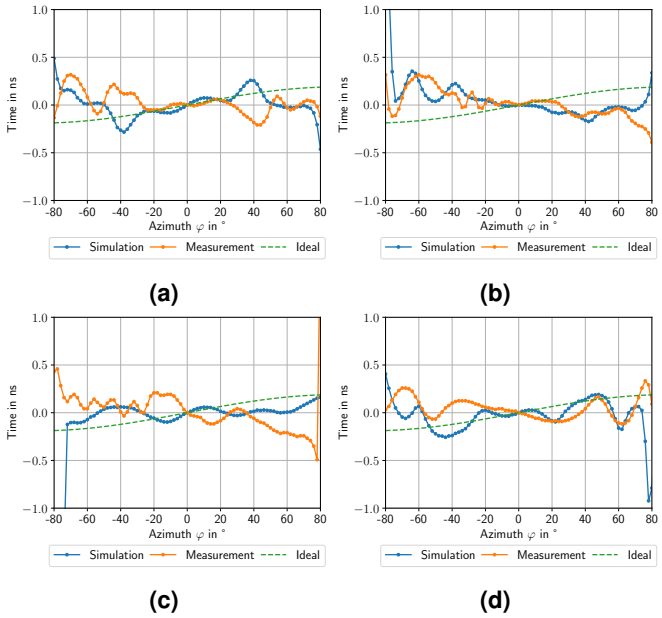

Figure 25: Comparison of simulated and measured TDoA curves over azimuth φ for the XETS antenna pair, measured at UWB channel 5. Subplot (a) shows the PDoA curves for $\theta = 0°$, (b) for $\theta = 30°$, (c) for $\theta = 60°$, and (d) for $\theta = -30°$.

1. **Linear polarization**: $\phi_\varphi - \phi_\theta \in \{0, \pi\}$
2. **Circular polarization**: $P_\varphi = P_\theta$
   - Counter clockwise rotation: $\phi_\varphi - \phi_\theta = -\frac{\pi}{2}$
   - Clockwise rotation: $\phi_\varphi - \phi_\theta = \frac{\pi}{2}$
3. **Elliptical polarization**: $P_\varphi \neq P_\theta$
   - Counter clockwise rotation: $\phi_\varphi - \phi_\theta = -\frac{\pi}{2}$
   - Clockwise rotation: $\phi_\varphi - \phi_\theta = \frac{\pi}{2}$

The incident wave direction $\boldsymbol{n}^{+}$ itself is expressed in terms of the two angles azimuth φ and elevation θ. The definitions of φ and θ do not follow the common definitions in a spherical coordinate frame, but were selected to meet the rotations applied by the 6-axis robot used during measurement (see Figure 6). The 6 axis robot acts as a *elevation-over-azimuth* positioner [33], with the elevation rotation carried out first, as a rotation by θ degrees around the AUTs negative x-axis. The subsequent azimuth rotation is then carried out by rotation of φ degrees around the y-axis of the previously rotated coordinate frame. The rotation operations can be described by means of the two rotation matrices $\boldsymbol{R}_{\text{Elevation}}(\theta)$, $\boldsymbol{R}_{\text{Azimuth}}(\varphi)$ [41, Ch. 2]

$$\boldsymbol{R}_{\text{Elevation}}(\theta) = \begin{bmatrix} 1 & 0 & 0 \\ 0 & \cos(\theta) & \sin(\theta) \\ 0 & -\sin(\theta) & \cos(\theta) \end{bmatrix} \quad (55)$$

$$\boldsymbol{R}_{\text{Azimuth}}(\varphi) = \begin{bmatrix} \cos(\varphi) & 0 & \sin(\varphi) \\ 0 & 1 & 0 \\ -\sin(\varphi) & 0 & \cos(\varphi) \end{bmatrix}\ ,$$

leading incident wave direction $\boldsymbol{n}^+$ expressed in terms of azimuth φ and elevation θ

$$\boldsymbol{n}^+(\varphi,\theta) = \boldsymbol{R}_{\text{Elevation}}(\theta)\,\boldsymbol{R}_{\text{Azimuth}}(\varphi)\begin{bmatrix}0\\0\\1\end{bmatrix} = \tag{56}$$
$$= \begin{bmatrix}\sin(\varphi)\\ \sin(\theta)\cos(\varphi)\\ \cos(\theta)\cos(\varphi)\end{bmatrix}.$$

Consequently, the unit vectors in azimuth and elevation direction, $\boldsymbol{i}_\varphi$ and $\boldsymbol{i}_\theta$ are obtained in terms of φ and θ as

$$\boldsymbol{i}_\varphi(\varphi,\theta) = \boldsymbol{R}_{\text{Elevation}}(\theta)\,\boldsymbol{R}_{\text{Azimuth}}(\varphi)\begin{bmatrix}1\\0\\0\end{bmatrix} = \tag{57}$$
$$= \begin{bmatrix}\cos(\varphi)\\ -\cos(\theta)\sin(\varphi)\\ -\cos(\theta)\sin(\varphi)\end{bmatrix},$$

$$\boldsymbol{i}_\theta(\varphi,\theta) = \boldsymbol{R}_{\text{Elevation}}(\theta)\,\boldsymbol{R}_{\text{Azimuth}}(\varphi)\begin{bmatrix}0\\1\\0\end{bmatrix} = \tag{58}$$
$$= \begin{bmatrix}0\\ \cos(\theta)\\ -\sin(\theta)\end{bmatrix}.$$

The propagation vector $\boldsymbol{k}^+$ of the incident plane wave points in the negative radial direction $\boldsymbol{i}_r$ of the AUTs coordinate frame, as shown in Figure 26. Hence, the azimuth component $\tilde{P}_\varphi$ of polarization $\tilde{\boldsymbol{P}}$ from (54) still specifies the azimuth component $\tilde{E}_\varphi$ of the electric field strength. But the respective elevation component $\tilde{P}_\theta$ determines the negative electric field component $-\tilde{E}_\theta$, because the elevation direction $\boldsymbol{i}_\theta$ of the AUT points in the opposite direction to $\boldsymbol{i}_{\tilde{E}_\theta}$.

B. PDoA and TDoA relations for planar arrays

In this section, the TDoA and PDoA relations from (48) and (49) are rephrased for planar arrays like the one depicted in Figure 26, under the coordinate system conventions from Appendix A. The derivations also apply for linear arrays, as a special case of planar arrays. For a planar array, the positions of two arbitrary antennas m and n are

$$\Delta\boldsymbol{q}_n = \begin{bmatrix}x_n\\y_n\\0\end{bmatrix}, \quad \Delta\boldsymbol{q}_m = \begin{bmatrix}x_m\\y_m\\0\end{bmatrix}. \tag{59}$$

The respective position delta $\Delta\boldsymbol{q}_n - \Delta\boldsymbol{q}_m$ required in (48) and (49) is

$$\Delta\boldsymbol{q}_n - \Delta\boldsymbol{q}_m = \begin{bmatrix}x_n\\y_n\\0\end{bmatrix} - \begin{bmatrix}x_m\\y_m\\0\end{bmatrix} := \begin{bmatrix}\Delta x_{nm}\\ \Delta y_{nm}\\0\end{bmatrix}. \tag{60}$$

Finally expressing the incident wave direction $\boldsymbol{n}^+$ in terms of azimuth φ and elevation θ as shown in (56) in Appendix A, one

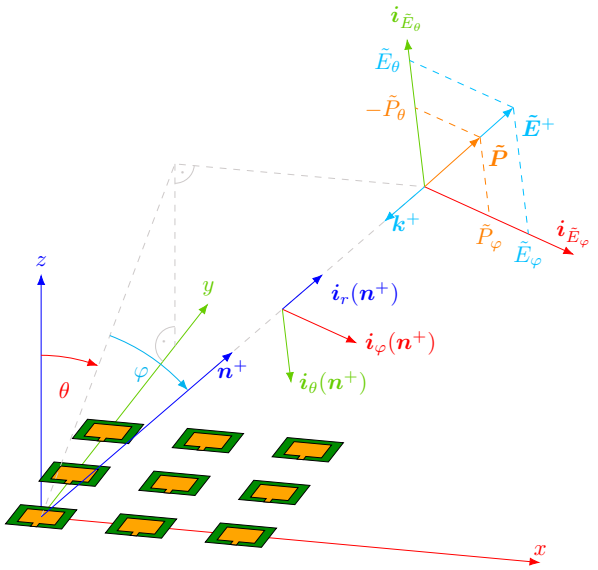

Figure 26: Geometric considerations for consistently modelling incident plane waves on the AUT in simulation and measurement. During measurement, the positioner rotates the antenna by azimuth φ and elevation θ, and the reference antenna is aligned to the respective unit vectors $\boldsymbol{i}_\varphi$ and $\boldsymbol{i}_\theta$. To model a consistent plane wave in simulation, its electric field strength $\tilde{\boldsymbol{E}}^+$ is defined with respect to the unit vectors $\boldsymbol{i}_{\tilde{E}_\varphi}$ and $\boldsymbol{i}_{\tilde{E}_\theta}$, and subsequently transformed to the antenna coordinate frame (xyz) using the rotation matrices (55).

obtains for the PDoA and TDoA between antennas m and n

$$\Delta\tau_{nm} = -\frac{1}{c_0}\left[\Delta x_{nm}\sin(\varphi) + \Delta y_{nm}\sin(\theta)\cos(\varphi)\right] + \hat{\tau}_n - \hat{\tau}_m \tag{61}$$

$$\Delta\Phi_{nm} = \frac{2\pi}{\lambda}\left[\Delta x_{nm}\sin(\varphi) + \Delta y_{nm}\sin(\theta)\cos(\varphi)\right] + \hat{\phi}_n - \hat{\phi}_m, \tag{62}$$

which are the well-known PDoA and TDoA relations for narrowband and wideband antenna arrays e.g. from [9], extended by the impact of the receive antennas.

References

[1] T. Wilding, S. Grebien, U. Mühlmann, and K. Witrisal, "Accuracy Bounds for Array-Based Positioning in Dense Multipath Channels," *Sensors*, vol. 18, no. 12, p. 4249, Dec. 2018. doi: 10.3390/s18124249

[2] Y. Han, Y. Shen, X.-P. Zhang, M. Z. Win, and H. Meng, "Performance Limits and Geometric Properties of Array Localization," *IEEE Transactions on Information Theory*, vol. 62, no. 2, pp. 1054–1075, Feb. 2016. doi: 10.1109/TIT.2015.2511778

[3] Y. Shen and M. Z. Win, "Fundamental Limits of Wideband Localization— Part I: A General Framework," *IEEE Transactions on Information Theory*, vol. 56, no. 10, pp. 4956–4980, Oct. 2010. doi: 10.1109/TIT.2010.2060110

[4] David Veit, "Characterization, Verification and Optimization of Ultra-Wideband Impulse Radio Ranging Systems," Ph.D. dissertation, Graz University of Technology, Graz, Aug. 2020. doi: 10.3217/93tps-75w92

[5] D. Manteuffel, T. Ould, and T. Kempka, "Antenna and propagation impairments of a UWB localization system integrated into an aircraft cabin," in *2010 Loughborough Antennas & Propagation Conference*. Loughborough, United Kingdom: IEEE, Nov. 2010, pp. 589–592. doi: 10.1109/LAPC.2010.5666904. ISBN 978-1-4244-7304-5

[6] W. Sörgel and W. Wiesbeck, "Influence of the Antennas on the Ultra-Wideband Transmission," *EURASIP Journal on Advances in Signal Processing*, vol. 2005, no. 3, p. 843268, Dec. 2005. doi: 10.1155/ASP.2005.296

[7] W. Gerok, M. El-Hadidy, S. A. El Din, and T. Kaiser, "Influence of the real UWB antennas on the AoA estimation based on the TDoA localization technique," in *IEEE Middle East Conference on Antennas and Propagation (MECAP 2010)*. Cairo, Egypt: IEEE, Oct. 2010, pp. 1–6. doi: 10.1109/MECAP.2010.5724210. ISBN 978-1-61284-903-4

[8] I. Oppermann, M. Hämäläinen, and J. Iinatti, Eds., *UWB Theory and Applications*, 1st ed. Wiley, Sep. 2004. ISBN 978-0-470-86917-8 978-0-470-86919-2

[9] I. Dotlic, A. Connell, H. Ma, J. Clancy, and M. McLaughlin, "Angle of arrival estimation using decawave DW1000 integrated circuits," in *2017 14th Workshop on Positioning, Navigation and Communications (WPNC)*. Bremen: IEEE, Oct. 2017, pp. 1–6. doi: 10.1109/WPNC.2017.8250079. ISBN 978-1-5386-3089-1

[10] S. Diagne, T. Val, A. K. Farota, B. Diop, and O. Assogba, "Performances Analysis of a System of Localization by Angle of Arrival UWB Radio," *International Journal of Communications, Network and System Sciences*, vol. 13, no. 02, pp. 15–27, 2020. doi: 10.4236/ijcns.2020.132002

[11] R. Juran, P. Mlynek, M. Stusek, P. Masek, M. Mikulasek, and A. Ometov, "Hands-On Experience with UWB: Angle of Arrival Accuracy Evaluation in Channel 9," in *2022 14th International Congress on Ultra Modern Telecommunications and Control Systems and Workshops (ICUMT)*. Valencia, Spain: IEEE, Oct. 2022, pp. 45–49. doi: 10.1109/ICUMT57764.2022.9943504

[12] J. Krška, C. Gentner, and V. Navrátil, "Angle of Arrival Measurements with Ultra-wide Band Transceivers: Design and Evaluation," in *2024 18th European Conference on Antennas and Propagation (EuCAP)*. Glasgow, United Kingdom: IEEE, Mar. 2024, pp. 1–5. doi: 10.23919/EuCAP60739.2024.10501361. ISBN 978-88-312-9909-1

[13] T. Margiani, S. Cortesi, M. Keller, C. Vogt, T. Polonelli, and M. Magno, "Angle of Arrival and Centimeter Distance Estimation on a Smart UWB Sensor Node," *IEEE Transactions on Instrumentation and Measurement*, pp. 1–11, 2023. doi: 10.1109/TIM.2023.3282289

[14] C. Baum, "General properties of antennas," *IEEE Transactions on Electromagnetic Compatibility*, vol. 44, no. 1, pp. 18–24, Feb. 2002. doi: 10.1109/15.990707

[15] C. A. Balanis, *Antenna Theory: Analysis and Design*, 3rd ed. Hoboken, NJ: John Wiley, 2005. ISBN 978-0-471-66782-7

[16] E. Pancera, C. Sturm, J. Fortuny-Guasch, T. Zwick, and W. Wiesbeck, "Full 3D spatial time domain analysis of UWB antennas," in *2008 IEEE Antennas and Propagation Society International Symposium*. San Diego, CA: IEEE, Jul. 2008, pp. 1–4. doi: 10.1109/APS.2008.4619574. ISBN 978-1-4244-2041-4

[17] M. Kanda, "Time domain sensors for radiated impulsive measurements," *IEEE Transactions on Antennas and Propagation*, vol. 31, no. 3, pp. 438–444, May 1983. doi: 10.1109/TAP.1983.1143057

[18] G. Smith, "A Direct Derivation of a Single-Antenna Reciprocity Relation for the Time Domain," *IEEE Transactions on Antennas and Propagation*, vol. 52, no. 6, pp. 1568–1577, Jun. 2004. doi: 10.1109/TAP.2004.830257

[19] J. R. Costa, C. R. Medeiros, and C. A. Fernandes, "Performance of a Crossed Exponentially Tapered Slot Antenna for UWB Systems," *IEEE Transactions on Antennas and Propagation*, vol. 57, no. 5, 2009. doi: 10.1109/TAP.2009.2016727

[20] M. El-Hadidy, "UWB antennas: Mathematical presentation, Impulse Response simulation and Electromagnetic modeling," in *2013 International Conference on High Performance Computing & Simulation (HPCS)*. Helsinki, Finland: IEEE, Jul. 2013, pp. 357–361. doi: 10.1109/HPCSim.2013.6641439

[21] J.-H. Kim and D.-H. Kwon, "Effective Heights for Array Antennas for Radiation and Reception Characterization," in *2024 IEEE International Symposium on Antennas and Propagation and INC/USNC-URSI Radio Science Meeting*. Firenze, Italy: IEEE, Jul. 2024, pp. 945–946. doi: 10.1109/AP-S/INC-USNC-URSI52054.2024.10686531

[22] A. Shlivinski, E. Heyman, and R. Kastner, "Antenna characterization in the time domain," *IEEE Transactions on Antennas and Propagation*, vol. 45, no. 7, pp. 1140–1149, Jul. 1997. doi: 10.1109/8.596907

[23] H. Krim and M. Viberg, "Two decades of array signal processing research: The parametric approach," *IEEE Signal Processing Magazine*, vol. 13, no. 4, pp. 67–94, Jul. 1996. doi: 10.1109/79.526899

[24] A. Richter, R. Thomä, M. Haardt, and E. Bonek, "Estimation of Radio Channel Parameters: Models and Algorithms," Ph.D. dissertation, ISLE, Ilmenau, 2005.

[25] T. Pedersen, "Contributions in Radio Channel Sounding, Modeling, and Estimation," Ph.D. dissertation, Department of Electronic Systems, Aalborg University, Aalborg, 2009.

[26] D. Dardari, A. Conti, U. Ferner, A. Giorgetti, and M. Z. Win, "Ranging With Ultrawide Bandwidth Signals in Multipath Environments," *Proceedings of the*

IEEE, vol. 97, no. 2, pp. 404–426, Feb. 2009. doi: 10.1109/JPROC.2008.2008846

[27] C. Falsi, D. Dardari, L. Mucchi, and M. Win, "Range Estimation in UWB Realistic Environments," in *2006 IEEE International Conference on Communications*. Istanbul: IEEE, 2006, pp. 5692–5697. doi: 10.1109/ICC.2006.255571

[28] "Ansys HFSS | 3D High Frequency Simulation Software," https://www.ansys.com/products/electronics/ansys-hfss, accessed 2024-06-05.

[29] "IEEE standard for low-rate wireless networks," *IEEE Std 802.15.4-2020 (Revision of IEEE Std 802.15.4-2015)*, pp. 1–800, 2020. doi: 10.1109/IEEESTD.2020.9144691

[30] E. Pancera, T. Zwick, and W. Wiesbeck, "Spherical Fidelity Patterns of UWB Antennas," *IEEE Transactions on Antennas and Propagation*, vol. 59, no. 6, pp. 2111–2119, Jun. 2011. doi: 10.1109/TAP.2011.2143666

[31] K. M. M. Prabhu, *Window Functions and Their Applications in Signal Processing*. Boca Raton, [Florida]: CRC Press/Taylor & Francis, 2014. ISBN 978-1-4665-1583-3

[32] Dobot, "Nova 5," https://www.dobot-robots.com/products/nova-series/nova5.html, accessed 2025-02-26.

[33] G. F. Masters and S. F. Gregson, "Coordinate system plotting for antenna measurements," in *AMTA Annual Meeting & Symposium*, vol. 32, 2007.

[34] J. Jaeger, R. Moch, T. M. Gemmer, and D. Heberling, "Development of a Motion-Capable Model for a Robot-Based Antenna Measurement System to Simulate Scattering-Induced Interference," in *2021 Antenna Measurement Techniques Association Symposium (AMTA)*. Daytona Beach, FL, USA: IEEE, Oct. 2021, pp. 1–6. doi: 10.23919/AMTA52830.2021.9620538. ISBN 978-1-73623-511-9

[35] ETS-Lindgren, "3115 Double-Ridged Guide Antenna - ETS-Lindgren," https://www.ets-lindgren.com/products/antennas/double-ridged-guide/4002/400203?page=Products-Item-Page, accessed 2025-02-26.

[36] Keysight, "N9916B FieldFox Handheld Microwave Analyzer, 14 GHz," https://www.keysight.com/us/en/product/N9916B/fieldfox-b-handheld-microwave-analyzer-14-ghz.html, accessed 2025-02-26.

[37] ——, "N7553A Electronic Calibration Module (ECal), DC-14 GHz, 2-Port," https://www.keysight.com/us/en/product/N7553A/electronic-calibration-module-ecal-dc-14-ghz-2-port.html, accessed 2025-02-26.

[38] NXP Semiconductors, "Vivaldi Antenna for UWB Applications," https://www.nxp.com/products/wireless/secure-ultra-wideband-uwb/vivaldi-antenna-for-uwb-applications:LID2509, accessed 2024-06-05.

[39] A. F. Molisch, *Wireless Communications*, 2nd ed. Chichester: Wiley, 2011. ISBN 978-0-470-74187-0 978-0-470-74186-3

[40] Mini-Circuits, "1:1 CORE & WIRE Transformer, 10 - 8000 MHz, 50Ohm | SCTX1-83-2W+," https://www.minicircuits.com/WebStore/dashboard.html?model=SCTX1-83-2W%2B, accessed 2024-06-22.

[41] M. W. Spong, S. Hutchinson, and M. Vidyasagar, *Robot Modeling and Control*. Hoboken, N.J: Wiley, 2006. ISBN 978-0-471-64990-8